J Seismol (2022) 26:1105–1136
https://doi.org/10.1007/s10950-022-10114-8

ORIGINAL ARTICLE

Regional model of peak ground motion in Southwestern Germany

Jens Zeiß · Stefan Stange · Andrea Brüstle

Received: 4 April 2022 / Accepted: 27 September 2022 / Published online: 5 November 2022

Abstract Ground motion prediction equations (GMPEs) and the effects of site amplifications are substantial for the assessment of seismic hazard. To investigate the regional earthquake ground motion in southwestern Germany, we fit ground motion models to observed horizontal peak ground acceleration from earthquakes with $0.9 \leq M_L \leq 4$ using the earthquake catalogue of the joint federal seismological services of Baden-Württemberg and Rhineland-Palatinate (Erdbebendienst Südwest), Germany. We use GMPEs that consider first-order geometrical spreading, first-order magnitude-scaling, and apparent anelastic attenuation. Due to indications from the data residuals, we additionally introduce a heuristically defined expression to consider Mohorovičić reflection phases, and a second-order geometrical decay term that is derived to approximate the decay of a general moment-tensor source. While the expression for the Mohorovičić reflection phases improved the data fit, the second-order decay term is hardly changing the resulting model. Averaged site deviations from the median model are incorporated to account for site effects. Depending on the local geological conditions, these deviations show a strong variability within individual seismogeographical regions.

Keywords Regional peak ground motion prediction · Upper Rhine Graben · Southwestern Germany · Site amplification · Near-source geometrical spreading

1 Introduction

1.1 Tectonic setting and seismiciy in the study area

The study area is placed in Central Europe and covers parts of the Rhenish Massif, the Upper Rhine Graben (URG), the Southwest German Scarplands, and the western part of the German Alpine Foreland. The earthquake activity in Central Europe is considered to be moderate in comparison to the global level, whereby the stress field of this intraplate region is mainly controlled by colliding movements of the African continental plate towards the Eurasian continental plate (Grünthal and Stromeyer 1992; Müller et al. 1992; Ziegler 1994; Hinzen 2003; Heidbach et al. 2007; Reicherter et al. 2008). The predominant

Supplementary Information The online version contains supplementary material available at https://doi.org/10.1007/s10950-022-10114-8.

J. Zeiß · S. Stange · A. Brüstle
Regierungspräsidium Freiburg, Geological Survey of Baden-Württemberg, State Seismological Service, Freiburg, Germany

Present Address:
J. Zeiß (✉)
Geological Survey of North Rhine-Westphalia, State Seismological Service, Krefeld, Germany
e-mail: jens.zeiss@gd.nrw.de

focal mechanism in the study area is strike-slip, but also normal-faulting events are observed.

Figure 1 shows the seismogeographical regions (Table 1; after Leydecker and Aichele 1998; Leydecker 2011) as well as the epicenters of the earthquakes used in this study. Natural earthquakes are mostly observed at the Ochtendung Fault Zone (c.f. Ahorner 1983) with the East Eifel Volcanic Field (c.f. Hensch et al. 2019) in the Middle Rhine Area (MR), along the URG (NR, SR) including its graben shoulders (especially the Southern Black Forest, SW), at the western Lake Constance Region (BO), and along the Albstadt Shear Zone (c.f. Schneider 1979) on the Swabian Jura (SA).

The largest known event north of the Alpine region is the so-called Basel-earthquake in 1356 with a maximum intensitiy I_0 of VIII and a moment magnitude M_W in the range between 6.7 and 7.1 (Fäh et al. 2009). Other major earthquakes occured at St. Goar/MR in 1846 ($M_L = 5.5$; $M_W = 5.0$; I_0 =VII; Leydecker 2011), at Waldkirch/SW in 2004 ($M_L = 5.4$; I_0 = VI - VII), and at Albstadt/SA in 1911 ($M_L = 6.1$), in 1943 ($M_L = 5.5$) and in 1978 ($M_L = 5.7$) with intensitites ranging from VII to VIII (Brüstle et al. 2015).

Additionally, also induced seismicity caused by several deep geothermal projects within the URG became increasingly important in the recent years. For instance, earthquakes with magnitudes up to

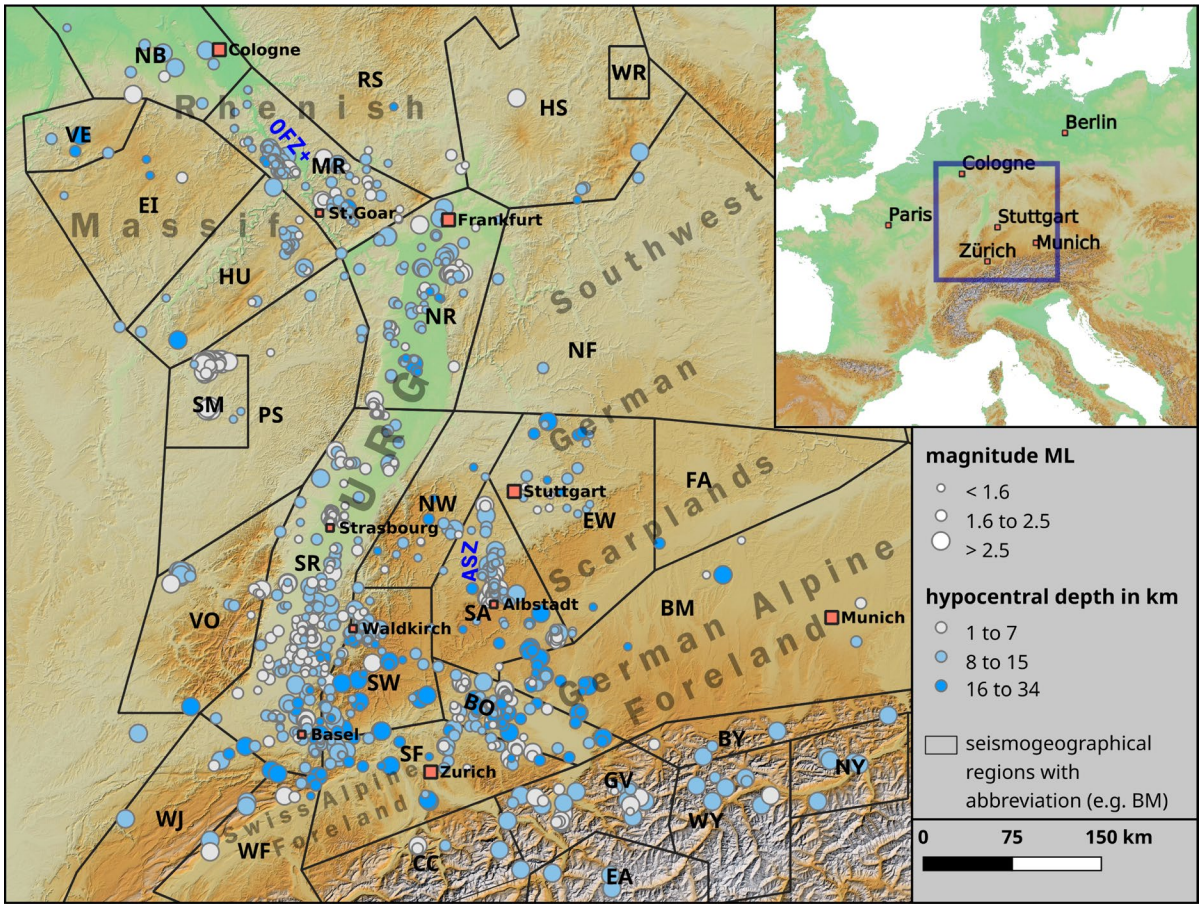

Fig. 1 Map of the study area with the epicenters of the earthquakes, for which PGA-values are determined. Abbreviations of the seismogeographical regions as defined by Leydecker (2011) are explained in Table 1. The epicenters are displayed according to the catalogue of the joint seismological services of the German federal states Baden-Württemberg and Rhineland-Palatinate. Furthermore, the main geological units and the locations of selected seismic zones are approximately indicated: Upper Rhine Graben (URG), Albstadt Shear Zone (ASZ), Ochtendung Fault Zone with East Eifel Volcanic Field (OFZ+)

Table 1 The seismogeographical regions (according to Leydecker 2011 and Leydecker and Aichele 1998) of the study area and their abbreviations. Number of PGA-values associated with the respective source region

Abbreviation	Seismogeographical region	Number of PGA-values
BM	Bavarian Molasse Basin	336
BO	Lake Constance Region	2864
BY	Bavarian Alps	6
CC	Central Switzerland	44
EA	Eastern Swiss Alps	26
EI	Eifel Mountain Region	92
EW	Eastern Württemberg	341
FA	Frankonian Jura	12
GV	St. Gall and Vorarlberg	218
HU	Hunsrück	281
HS	Hessian Depression	34
MR	Middle Rhine Area	2075
NB	Lower Rhine Area	109
NF	Northern Frankonia	21
NR	Northern Upper Rhine Graben	1092
NW	Northern Black Forest	236
NY	Northeastern Tyrol	13
PS	Pfalz-Saar Area	94
RS	Eastern Rhenish Massif	64
SA	Swabian Jura	2710
SF	Eastern Swiss Alpine Foreland	471
SM	Saar Mining District	219
SR	Middle and Southern Upper Rhine Graben	5922
SW	Southern Black Forest	1291
VE	Venn Area	40
TC	Central Thuringia	5
VO	Vosges Mountain Region	327
WJ	Western Jura	31
WF	Western Swiss Alpine Foreland	106
WY	Western Jura	49
F	others in France	47

$M_L = 3.4$ at Basel (Häring et al. 2008; Kraft and Deichmann 2014) or $M_L = 4.0$ near Strasbourg (Schmittbuhl et al. 2020, 2021) were observed.

1.2 Ground motion predictions

A ground motion prediction equation (GMPE) predicts expected measures of ground motion including their uncertainty from several predictor variables which represent given values like earthquake magnitude or source-to-site distance. The functional forms between available GMPEs for crustal earthquakes differ considerably. Some GMPEs are based on physically reasoned functional forms, and others use any heuristically defined functions to reproduce the observations.

Recently developed GMPEs based on global data commonly include terms which account for many effects influencing ground motions: non-linear magnitude-scaling, magnitude-dependent geometrical decay, style of faulting, regional dependent apparent anelastic attenuation, thickness of surfical

sedimentary layers, depth of the rupture, hanging wall effects, fault dip, or rupture directivity. Exemplary GMPEs considering most of these factors were developed by Abrahamson et al. (2014); Boore et al. (2014) and Campbell and Bozorgnia (2014).

GMPEs based on regional data and weak earthquakes rather use simpler models because the data do not allow to quantify all of these effects or because the considered magnitude and distance ranges allow certain simplifications. For instance, GMPEs modelling only weak earthquakes mostly assume a linear magnitude-dependency and a simple geometrical distance-decay. In contrast, in case of larger earthquakes and broad magnitude ranges, a non-linear magnitude-dependency is needed and a further magnitude-dependent distance-decay is considered. This is also the case for several GMPEs for Europe and the Middle East, e.g. those by Ambraseys et al. (2005) or Bindi et al. (2014).

The used predictor variables also vary with the models. Most important are the predictor variables that describe the distance to the source and the strength of the earthquake. To avoid the saturation of most magnitude scales, the moment magnitude is commonly used. The distance to the source is typically measured by means of the Joyner-Boore distance (distance to the surface projection of the rupture; Boore and Joyner 1982) or the closest distance to the rupture plane. Both the hypocentral and the epicentral distance are rather used in the case of predictions for weak earthquakes. Further variables are needed, if detailed source characteristics (e.g. focal mechanism, directivity, dip of the rupture, depth to the top of the rupture plane, stress drop), specific properties along the wave paths (regional dependent apparent anelastic attenuation and reflections/refractions from discontinuities), and site properties near the surface should be incorporated.

An application of available ground motion models in context of seismic hazard assessments demands for various requirements. To select an existing model for a target region, e.g. Cotton et al. (2006) and Bommer et al. (2010) formulated several criteria considering topics such as the tectonic environment, the functional form, the form of publication, the data quality, and the data access. However, the particularities of ground motion in regions with moderate seismicity are often not satisfyingly known. Furthermore, it is questionable, if models from active tectonic regions or stable continental regions should preferentially be used for intraplate regions with moderate seismicity. This is also the case for southwestern Germany. According to a classification by Chen et al. (2018), the study area is mainly classified as an active region, but partially as a stable non-craton region.

1.3 Research objectives

In this study, we investigate the local characteristics of ground motion in southwestern Germany considering weak to moderate earthquakes. Hereby, we at first make use of the earthquake catalogue of the joint seismological services of the German federal states Baden-Württemberg and Rhineland-Palatinate (Erdbebendienst Südwest EDSW). We extract peak ground acceleration (PGA) values from the corresponding instrumental recordings of the local earthquakes with M_L between 0.9 and 4, and fit GMPEs with varying functional forms to the observed PGA. Besides the very common terms that consider first-order geometrical spreading, first-order magnitude-scaling, we test second-order terms of geometrical spreading and a heuristically defined term to account for Mohorovičić reflections. Furthermore, station corrections are incorporated into the GMPE to measure site amplifications which are subsequently examined in the geological context.

The applicability of the resulting GMPEs to predict ground motion of moderate to strong earthquakes in context of seismic hazard analysis will be limited due to the lack of recordings from strong earthquakes in the study region. An expansion of models for stronger earthquakes will be speculative due to deviating magnitude-scaling and deviating decays with distance at different magnitude ranges. According to investigations by Douglas (2003); Douglas and Jousset (2011), or Baltay and Hanks (2014), models derived from data of small earthquakes show a higher dependency on magnitude than models derived from data of large earthquakes. As stated by Douglas and Edwards (2016), differing characteristics of the distance-decay result from constructive interference effects of a finite source (Boore 2009), from near field saturation and from differing spectral shapes (Cotton et al. 2008). Also, an expansion of the prediction of PGA to spectral accelarations including lower frequencies will be critical due to freuqency-dependent wave propagation effects, for instance due to

frequency-dependent anelastic attenuation (c.f McNamara 2000; Kotha et al. 2020). Correspondingly, nearly all the coefficients of the model by Bindi et al. (2014) show a significant dependency on frequency. However, we believe that the comprehensive set of earthquakes with low magnitudes allow to investigate local particularities of ground motion and provide an approximate measure of site amplifications within the region.

2 Data

2.1 Earthquake source data

From the bulletin of the EDSW, we used local tectonic and induced/triggered earthquakes. For the years 2010 through 2017, events with local magnitudes $2 \leq M_L \leq 4$ were extracted, and for the years 2018 and 2019 events with $0.9 \leq M_L \leq 4$ were used (Fig. 1). For these events, the location routine HYPOPLUS, a HYPO71 (Lee and Lahr 1972) derivative by Oncescu et al. (1996) with adaptive 1D velocity models, was applied in the routine observatory praxis. The seismic network of the EDSW consisted of about 30 online stations and some dial-up stations in the year 2010, but the number increased to more than 60 stations in 2019. Today, the seismic network is complemented with about 40 permanent stations from other agencies, mainly from the Swiss Seismological Service (SED) and the French Seismological and Geodetic Network (Résif-RLBP), and with several mostly temporary installed stations from the Karlsruhe Institute of Technology (Ritter 2017; Ritter et al. 2019) and the AlpArray working group (2015). The stations are predominantly placed near the seismically most active areas. Strong motion stations are used as well as high-gain stations. See more details regarding the seismic network in the Section 9 and in Table 4.

The local magnitudes M_L^{BW} (BW: Baden-Württemberg) of the earthquake catalogue are determined based on the relation by Stange (2006):

$$M_L^{BW} = \log_{10}\left(PGD^{WA}\right) + 1.11 \cdot \log_{10}(r) + 0.95 \cdot 10^{-3} \cdot r + 0.69. \quad (1)$$

Hereby, $\log_{10}$ is the logarithm to base 10. PGD^{WA} is the peak ground displacement as mean-to-peak amplitude of a simulated Wood-Anderson seismometer. r is the hypocentral distance.

The local magnitudes are converted to pseudo moment magnitudes using empirical relations by Edwards et al. (2010) and Deichmann (2017). Edwards et al. (2010) determined the relation

$$M_W = 1.02 + 0.472 \cdot M_L^{SED} + 0.0491 \cdot M_L^{SED\,2} \pm 0.15 \quad (2)$$

between local magnitudes ($1.3 < M_L^{SED} < 5.3$) and moment magnitudes. Hereby, the moment magnitudes are derived through a spectral fitting method and M_L^{SED} are the local magnitudes from the SED. Years of expierience let us assume that $M_L^{BW} \approx M_L^{SED}$ and use Eq. 2 to determine pseudo moment magnitudes from the local magnitudes of the EDSW.

To expand the moment magnitude estimation to weaker events with $M_L < 1.3$, we use the scaling relation

$$\frac{M_L}{M_W} = \frac{3}{2} \quad (3)$$

derived by Deichmann (2017) for events with magnitudes below a certain threshold. We integrate this scaling relation into Eq. 2 for local magnitudes below the threshold of $M_L = 2$ where the slope $\frac{\partial M_L}{\partial M_W}$ of Eq. 2 equals $\frac{3}{2}$. Finally, we apply

$$M_W = \begin{cases} \frac{2}{3} \cdot M_L^{BW} + 0.8267 & \text{for: } M_L^{BW} \leq 2 \\ 1.02 + 0.472 \cdot M_L^{BW} + 0.0491 \cdot M_L^{BW\,2} \pm 0.15 & \text{for: } M_L^{BW} > 2 \end{cases} \quad (4)$$

to determine pseudo moment magnitudes from the local magnitudes of the earthquake catalogue of the EDSW.

2.2 PGA extraction

The waveform data are available as event data with a typical length of 2 to 3 min. Traces from high-gain seismometers and strong-motion accelerometers are used. The sampling rates are predominantly set up at 100 Hz (high-gain instruments) and 200 Hz (strong-motion instruments).

The PGA-values are extracted by means of the following steps in an automatic procedure: The linear trends were removed, a band-pass filter from 1 to 35 Hz was applied, velocity traces were differentiated, the vector sum of horizontal acceleration was calculated sample for sample, and finally the maximum absolute values were extracted. To reject traces that

are masked by noise, we estimated the noise level from a time window before the first arrivals.

The resulting data set consists of about $N = 19100$ extracted PGA-values from more than 1200 earthquakes and about 110 stations (Fig. 2, Table 4). Hereby, only stations with at least 14 extracted PGA-values are considered.

The amount of data is unequally distributed with respect to source region, hypocentral distance, and magnitude (cf. Figs. 1, 3, and 4). Most PGA-values are associated with earthquakes in the regions SR, BO, SA, MR, SW, and NR (about 1000 to 6000 values each), whereas in others only a few PGA-values are extracted (see Table 1). Figures 3 and 4 show the number of PGA-values of a data subset (used during the optimisation of the coefficients; details in Section 4.1) with respect to the hypocentral distances and to the event magnitudes. Most PGA-values (300 to 700 values per 5-km-bin) are available within the hypocentral distance range from 25 to 125 km. At smaller and larger distances, the number of values decreases to about 50 per 5 km and 80 per 5 km. Regarding the magnitude distribution, we see that most PGA-values correspond to earthquakes with small magnitudes. From $M_W = 1.6$ to 2.3, about 1000 values are available within a magnitude bin (width of 0.1). The number of values decreases to roughly 100 values per bin for magnitudes of above 3.2. About 200 values are available for the magnitude bins between $M_W = 1.4$ and 1.6, respectively.

3 Investigated ground motion models

We test various functional forms using the ansatz

$$\log_{10}(\mathrm{PGA})_{e,s}^{\mathrm{pred}} = f_{\mathrm{geom}}(r_{e,s}, M_e) + f_{\mathrm{atn}}(r_{e,s}) + f_{\mathrm{Moho}}(r_{e,s}) + f_{\mathrm{M}}(M_e) + s_s + c \quad (5)$$

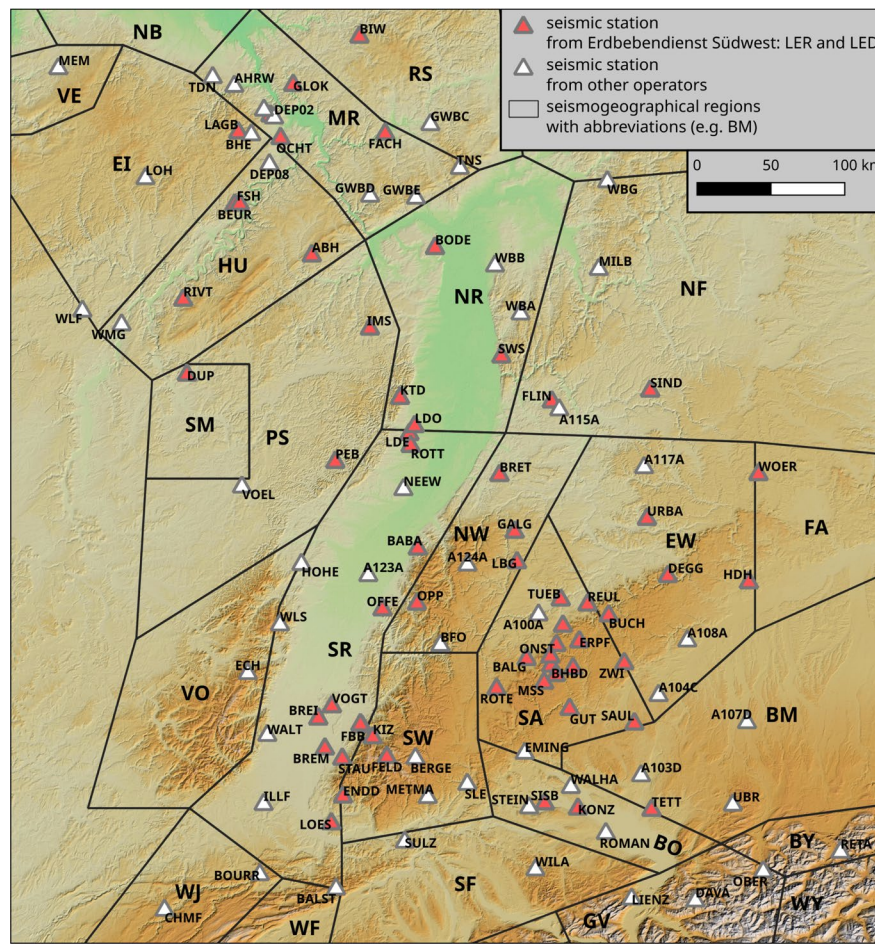

Fig. 2 Map of seismic stations for which PGA-values are determined. Seismogeographical regions as in Fig. 1 and Table 1

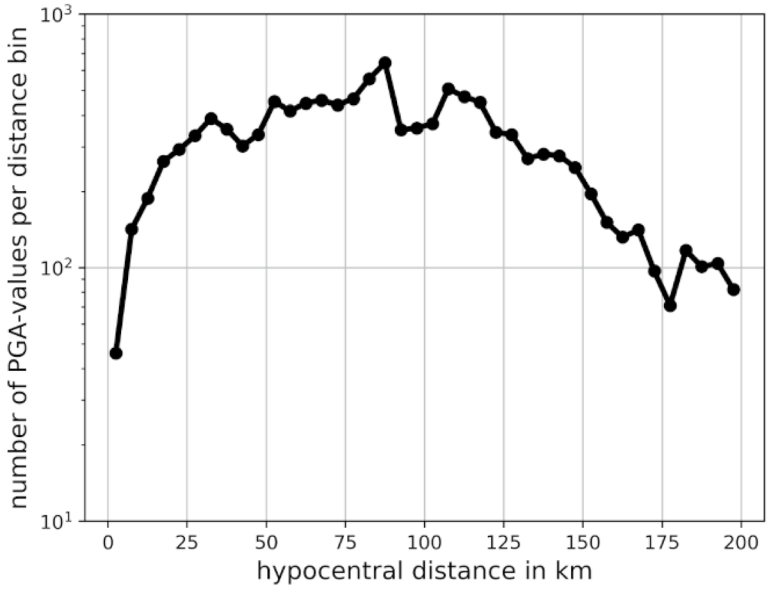

Fig. 3 Number of used PGA-values per distance bin (width of 5 km)

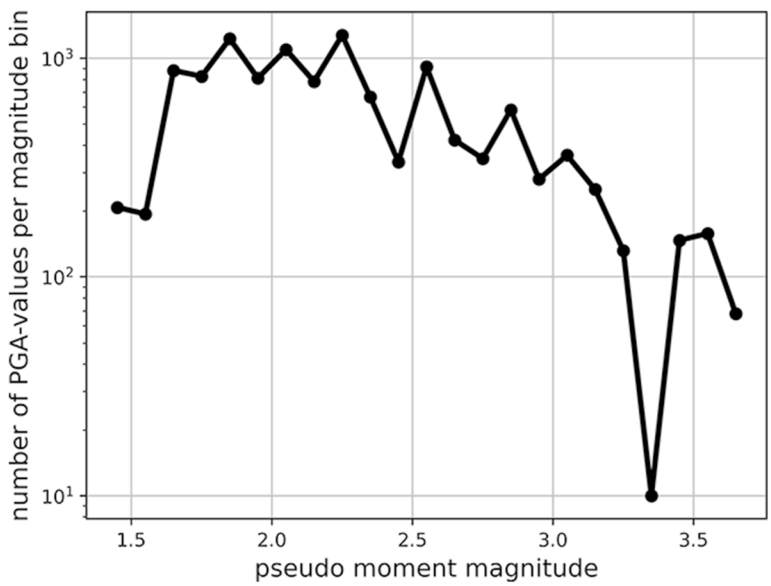

Fig. 4 Number of used PGA-values per magnitude bin (width of 0.1)

with $f_{\text{geom}}(r_{e,s}, M_e)$ to account for geometrical spreading, $f_{\text{atn}}(r_{e,s})$ for apparent anelastic attenuation (intrinsic attenuation and scattering), $f_{\text{Moho}}(r_{e,s})$ for Mohorovičić reflections and $f_{\text{M}}(M_e)$ for the PGA-increase with increasing event magnitude. c is a constant and s_s are station corrections to account for site effects. $\log_{10}(\text{PGA})^{\text{pred}}$ represents the predicted logarithm of PGA (PGA in m/s^2) and r is the hypocentral distance (in km) to a point source that is assumed. For the magnitude M, we use the pseudo

moment magnitudes (cf. Section 2.1). The indices e and s represent different events and stations.

3.1 Basic GMPE

Starting point is a GMPE which considers both simple geometrical spreading by defining

$$f_{\text{geom}}(r_{e,s}) = a\ \log_{10}(r_{e,s}) \tag{6}$$

and apparent attenuation by defining

$$f_{\text{atn}}(r_{e,s}) = b\, r_{e,s} \tag{7}$$

as functions of the hypocentral distance. In the case of a homogeneous, unbounded medium, the coefficient a equals -1.

For the magnitude-scaling, we assume a linear dependency:

$$f_{\text{M}}(M_e) = d \cdot M_e. \tag{8}$$

A quadratic dependency was also tested, but stability of the results and a significant variance reduction could not be achieved.

We refer to the resulting basic GMPE

$$\log_{10}(\text{PGA})^{\text{pred}}_{e,s} = a\ \log_{10}(r_{e,s}) + b\, r_{e,s} + c + d \cdot M_e + s_s \tag{9}$$

as GMPE$^{\text{basic}}$.

3.2 An expression for reflections from Mohorovičić discontinuity

Several studies have already reported or investigated the impact of the Mohorovičić discontinuity on observed peak amplitudes (e.g. Bakun and Joyner 1984; Burger et al. 1987; Mori and Helmberger 1996; Bragato et al. 2011; Sugan and Vuan 2012, 2014). However, to our knowledge, GMPEs which explicitly account for the observed impact are rare (e.g. Chiou and Youngs 2008, 2014).

After taking notice of strong Mohorovičić reflection phases for recorded earthquakes at Constance/BO in 2019 and because of the observed PGA-deviations (cf. Fig. 8) from the prediction of the GMPE$^{\text{basic}}$ in the distance range beween about 50 and 160 km, we introduce a heuristically defined term

$$f_{\text{Moho}}(r) = \begin{cases} \log_{10}\left(1 + g\ \sin^2\left(\frac{r - r_{\text{min}}}{r_{\text{max}} - r_{\text{min}}} \cdot \pi\right)\right) & \text{for: } r_{\text{max}} \geq r \geq r_{\text{min}} \\ 0 & \text{otherwise} \end{cases} \tag{10}$$

with $r_{\text{min}} = 50$ km and $r_{\text{max}} = 160$ km to account for energy reflected at the Mohorovičić discontinuity. The coefficient g scales the amplification within the distance range and will be determined during the inversion procedure. $g = 0$ corresponds to a vanished impact of the Mohorovičić term $f_{\text{Moho}}(r)$. We refer to corresponding GMPEs which contain $f_{\text{Moho}}(r)$ as GMPE$^{\text{Moho}}$.

It might be advantageous to consider r_{min} and r_{max} as a function of crustal thickness and source depth. However, we perferred in this study with data from a rather narrow area to begin with suitable values for the overall data set.

3.3 Intermediate wavefield approximation

As it can be seen later (Fig. 8), we do not recognise a near-source saturation at small hypocentral distances, what is typically observed on near-source recordings of stronger earthquakes. But a tendency of increasing residuals with decreasing hypocentral distance is present at small hypocentral distances ($r < 30$ km) when the models GMPE$^{\text{basic}}$ or GMPE$^{\text{Moho}}$ are applied. Hence, we introduce an additional term to model a steep PGA-decay at short distances.

We consider the intermediate and far S-wavefield of a general moment-tensor source as stated by Lokmer and Bean (2010) and allow several simplifications by (1) considering only the wavefield at predominant period T_0, (2) neglecting azimuthal dependency of source radiation patterns, (3) neglecting periodicities with number of wavelengths, (4) assuming that peak motion decay behaves mathematically as the full wavefield, and (5) using empirical relation between magnitude and predominant period T_0 (see details in Appendix A.5). Then, we get an alternative definition of the geometrical decay:

$$f_{\text{geom}}(r, M) = a\ \log_{10}(r) + \log_{10}\left(1 + z \cdot 10^{m \cdot M} \cdot r^{p}\right) \tag{11}$$

with $a = -1$, $p = -1$ for homogeneous unbounded media, $m \approx 0.5$ estimated from empirical relations between magnitude and predominant period T_0 (cf. values stated by Sato 1979), and $z = \frac{\beta}{2\pi} \cdot 10^{c'}$. β is the

S-wave velocity in km/s. c' is a constant which ranges between −1.2 and −2.6 in the empirical relations stated by Sato (1979).

Models which consider both a geometrical decay of Eq. 11 and a Mohorovičić reflection term will be tested. The corresponding GMPEs are named $\mathrm{GMPE}^{\mathrm{Moho,IS}}$.

4 Optimisation approach

4.1 Procedure

We apply the following three-phase optimisation procedure.

At the beginning of one iteration, we optimise the coefficients a, c, d, g, and z. During this phase A, we minimise the weighted cost function

$$C = \frac{1}{N}\sum_{i=1}^{N} w_i \cdot \left|\delta d_i\right| = \frac{1}{N}\sum_{i=1}^{N} w_i \cdot \left|\log_{10}(\mathrm{PGA})_i^{\mathrm{obs}} - \log_{10}(\mathrm{PGA})_i^{\mathrm{pred}}\right| \tag{12}$$

by applying the Trust Region Reflective algorithm (Branch et al. 1999; see Section 9). i is the increment of the data points; N is the number of the considered PGA-values. During phase A, only events are used, for which at least one PGA-value is available for distances below 80 km and simultaneously at least one PGA-value is available above 120 km. Thereby, the amount of PGA-values is reduced from more than 19,100 to about 11,900. The coefficients b (apparent anelastic attenuation), p (steepness of the decay near the source), and m (magnitude-dependency of the near-source-decay) will be fixed to the a priori values throughout all phases of the optimisation procedure.

Within the following phase B, we calculate station corrections s_s. These station corrections are achieved by computing the weighted median of the differences between the observed values $\log_{10}(\mathrm{PGA})^{\mathrm{obs}}$ and predicted values $\log_{10}(\mathrm{PGA})^{\mathrm{pred}}$ for each station respectively. Afterwards, the coefficient c and the median deviations are modified such that the sum of all median station corrections is zero. The station corrections should account for site effects which capture parts of within-event residuals (c.f. Atik et al. 2010). Further within-event residuals are caused by azimuthal variations in sources and by path effects.

To achieve magnitude corrections during phase C, we at first apply the ground motion models with the updated coefficients in a rearranged form to compute station magnitudes (event magnitudes as estimated from individual stations). Then, for each event, the median of the available station magnitudes is used to update the event magnitude. Magnitude corrections correspond to between-event residuals in the data domain (c.f. Atik et al. 2010). Other source effects (e.g. stress drop, style of faulting), which affect ground motion from earthquake to earthquake, might get projected into the pseudo moment magnitude. It is to mind that by incorporating magnitude corrections we allow adjustments of the predictor variable that controls ground motion adjustments from earthquake to earthquake.

We believe that the corrected magnitudes are less scattered compared to the initial local magnitude because the determined distance-decay of this study is based on a larger data set compared to the PGD-decay by Stange (2006). This also applies to the station corrections. However, the differences between the PGD- and PGA-amplitudes as well as the errors from applying the $M_{\mathrm{L}}^{\mathrm{BW}}$-$M_{\mathrm{W}}$-conversion are not assessed in this study. We denote the fitting parameters of phases B and C as magnitude corrections and station corrections to distinguish them from the coefficients a, b, c, d, g, z, and p.

4.2 Configurations

For the optimisation of the models, we perform eight iterations, whereby the magnitudes are first updated during iteration 4. The coefficients are initially set to $a = -1.1$, $b = -0.9 \cdot 10^{-3}$, $c = -4.2$, $d = 1$, $g = 0$, and $z = 0$. Hereby, a, b, and d are approximately chosen according to the modified Gutenberg-Richter attenuation curve for Baden-Württemberg by Stange 2006; cf. Eq. 1). $g = 0$ and $z = 0$ represent vanished impacts of the Mohorovičić term and of the second-order distance-decay.

We observed that the coefficent b could not be determined reliably (e.g. also physically not reasonable, positive values of b were determined using data subsets) probably for the following reasons. The amplitude decay at hypocentral distances up to about 100 km is mainly controlled by the geometrical decay and from about 50 to 160 km the decay is

also influenced by reflections from the Mohorovičić discontinuity. Such effects mask the impact of the anelastic attenuation and aggravates the determination of a physically reasonable value of b for our data set with a hypocentral distance limit at 200 km. Consequently, we fixed the b to the initial value of $-0.9 \cdot 10^{-3}$.

For the optimisation of the GMPE$^{\text{Moho,IS}}$, we fixed $m = 0.5$ and $p = -1$. This corresponds to the empirical and theoretical considerations of Section 3.3. Four iterations are performed, whereby the magnitude corrections from GMPE$^{\text{Moho}}$ are incorporated (and fixed) already at the beginning of the optimisation procedure.

4.3 Data weighting

The availability of data with respect to different source regions, hypocentral distances, and magnitude ranges differ considerably. We use data weights to balance the impacts of different source regions, hypocentral distances, and magnitude ranges. We define magnitude bins with a width of 0.1 and distance bins with a width of 5 km. We count the number of PGA-values that correspond to the individual bins. Additionally, we count the PGA-values of earthquakes that are located in the same seismogeographical region. Then, each PGA observation i is weighted by

$$w_{\text{coeff},i} = \frac{1}{N_{\text{reg},i}} \cdot \frac{1}{N_{\text{mag},i}} \cdot \frac{1}{N_{\text{dist},i}} \tag{13}$$

during the optimisation of the model coefficients (phase A) and by

$$w_{\text{sta},i} = \frac{1}{n_{\text{reg},i}} \tag{14}$$

during the computation of the station corrections (phase B). The numbers $N_{\text{reg},i}$, $n_{\text{reg},i}$, $N_{\text{mag},i}$, and $N_{\text{dist},i}$ are the counts of the PGA-values belonging to the same region, magnitude bin, or distance bin as the observation i.

The number $n_{\text{reg},i}$ differs from $N_{\text{reg},i}$ because for the optimisation of the coefficients (phase A) we decided to include only the earthquakes for which PGA-values from $r < 80$ km and $r > 120$ km are simultaneously available. But for the computation of station corrections, all PGA-values were used. To determine magnitude corrections (phase C), all available PGA-values of each event are used and weighted uniformly.

4.4 Bootstrap analysis

To estimate the statistical uncertainty for the coefficients of the model GMPE$^{\text{Moho}}$, a bootstrap analysis (c.f. Efron and Gong 1983) is performed with more than 250 replications. Each replication consists of the same number of data points as the original data set, whereby an individual data point can be selected repeatedly from the original data set. Data weights are recalculated according to Section 4.3 and based on the individual data set of each replication.

5 Optimisation results

5.1 Optimised median ground motion models

Figure 5 shows the misfit reduction in the case of the GMPE$^{\text{Moho}}$ after each iteration phase (A, B, C as described in Section 4.1). The misfit is measured using the weighted cost function $C_{w_{\text{coeff},i}}$ (with weights $w_{\text{coeff},i}$) and using the unweighted cost function $C_{w_i=1}$. The misfit is reduced by about 6% after the first optimisation. The introduction of station corrections reduces $C_{w_i=1}$ and $C_{w_{\text{coeff},i}}$ by about 20% of the initial values. From iteration 2 to phase B of iteration 4, $C_{w_i=1}$ and $C_{w_{\text{coeff},i}}$ do not change significantly. The introduction of magnitude corrections during the 4th iteration reduces $C_{w_i=1}$ and $C_{w_{\text{coeff},i}}$ from about 75 to about 62% of the initial values. No significant changes can be observed during the iterations 5 to 8.

Figure 6 illustrates the distance-decay and magnitude-scaling of the final model GMPE$^{\text{Moho,IS}}$ together with the data points. Table 2 (and Supplementary File 9) shows the coefficients and the unweighted cost function $C_{w_i=1}$ of the optimised models. The integration of the additional term $f_{\text{Moho}}(r)$ reduces $C_{w_i=1}$ by 10% with respect to the GMPE$^{\text{basic}}$. $C_{w_i=1}$ of the GMPE$^{\text{Moho,IS}}$ with $m = 0.5$ and $p = -1$ is reduced by about 0.1% with respect to $C_{w_i=1}$ of GMPE$^{\text{Moho}}$. The final misfit for GMPE$^{\text{Moho,IS}}$ measured using the standard deviation is $\sigma = \sqrt{\frac{1}{N}\sum_i \left|\delta d_i\right|^2} = 0.36$.

5.1.1 Distance-decay and the impact of f_{Moho}

The optimised geometrical decay coefficient a of the GMPE$^{\text{basic}}$ and the GMPE$^{\text{Moho}}$ lies at -1.61 and -1.59, whereby the 16th and the 84th bootstrap percentiles of

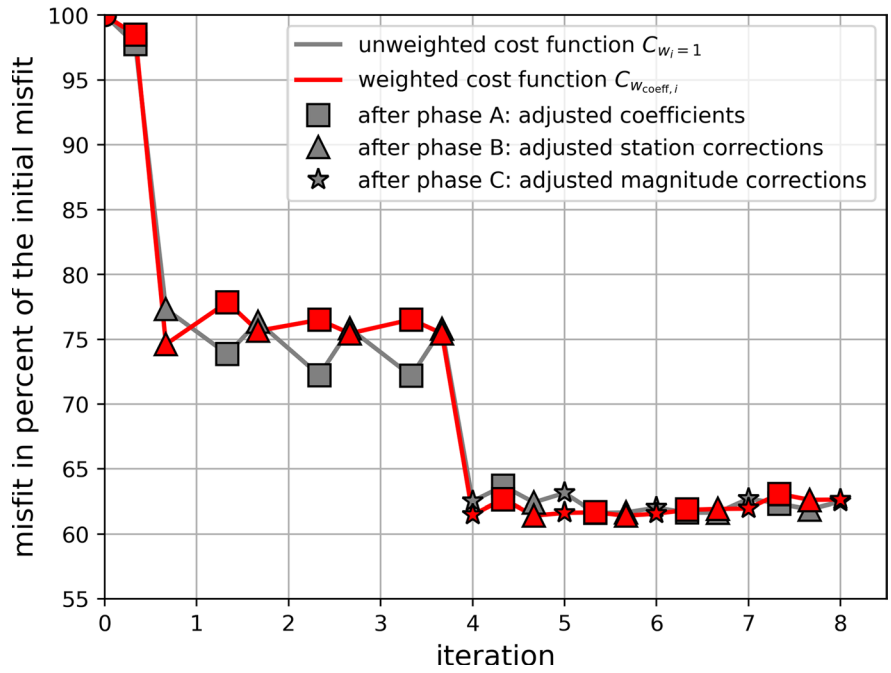

Fig. 5 Misfit after each iteration phase measured by $C_{w_i=1}$ and $C_{w_{\mathrm{coeff},i}}$ in percent to the initial misfit

Table 2 Final coefficients and the unweighted cost $C_{w_i=1}$ in $\log_{10}(\mathrm{m}/s^2)$. Fixed coefficients are bold. b is fixed to −0.0009 in any case

Model	a	c	d	g	z	p	C with $w_i = 1$
Basic	−1.61	−2.87	0.98	**0**	**0**	–	0.2215
Moho	−1.59	−3.47	1.12	0.61	**0**	–	0.1989
Moho IS	−1.58	−3.50	1.13	0.61	0.0054	**−1**	0.1987

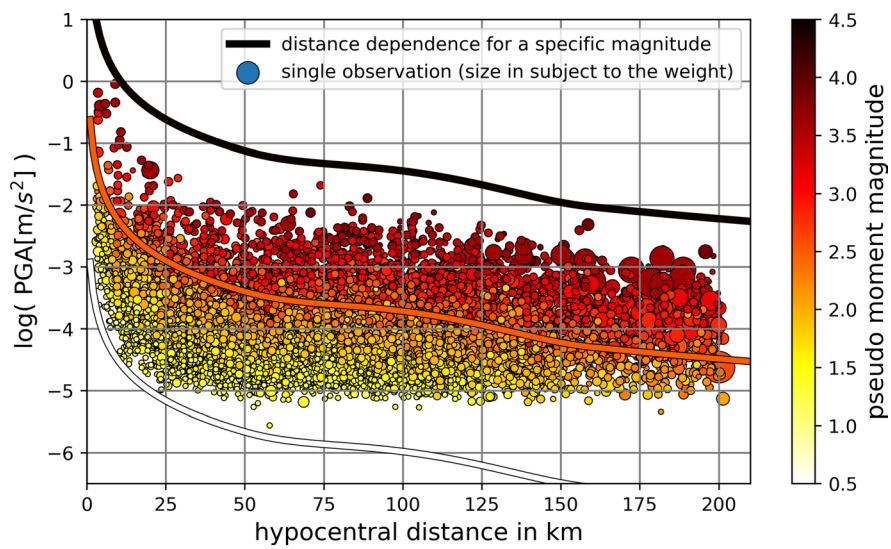

Fig. 6 Spatial PGA-decay of the averaged $\mathrm{GMPE}^{\mathrm{Moho,IS}}$ for moment magnitudes of 0.5, 2.5, and 4.5 as well as the observed PGA-values after applying the derived station corrections. Moment magnitudes after applying the magnitude corrections are colour-coded. The dot size is a function of the data weight

$\mathrm{GMPE}^{\mathrm{Moho}}$ are determined at −1.63 and −1.33. This result is consistent with the observed decay ($a \approx -1.5$) in the study of Frankel et al. (1990) who applied the reflectivity method (Kennett 1980; Kind 1977; Müller 1985) for SH seismograms from an isotropic source in a horizontally layered model.

The values of the regressed coefficient g are about 0.5 to about 0.6 which corresponds to a maximum amplitude $\max(f_{\mathrm{Moho}}(r)) = \log_{10}(1 + 0.6) = 0.2$ of Eq. 10 within the log-space. This corresponds to a PGA-amplification factor of 1.6. Optimisations with data subsets indicate a strong variability depending on the source region. Data with earthquakes only from SA or BO yield $g \approx 1.1$ (PGA-amplification factor of about 2.1). Data from MR, NR, and SR yield values of 0.3 to 0.5. In contrast, earthquakes from SW yield a value of $g \approx 0$ (cf. Table 5).

Considering the median models in Fig. 7, we see that increased PGA-values between hypocentral distances of about 75 and 130 km are predicted after including f_{Moho} in f_{geom}. Simultaneously, the median PGA-values below 75 km and above 130 km are decreased. The changes of the median curves are in the range of about ±0.1. In comparison, the changes due to the inclusion of the higher-order distance-decay are insignificant. Consequently, the use of the simpler Eq. 6 arises to be preferable to Eq. 11 for the given data set.

Figure 8 shows the distance-dependence of the residuals in the case of GMPE$^{\mathrm{basic}}$ and GMPE$^{\mathrm{Moho}}$. We can see that the tendency of rather positive residuals from 75 to 130 km could be reduced due to the term f_{Moho}. However, a tendency of negative residuals between 15 and 60 km in contrast to rather positive residuals at smaller and larger offsets remains.

5.1.2 *Uncertainty, local variability, and magnitude corrections*

For GMPE$^{\mathrm{Moho}}$, we determine the standard deviation on predicted $\log_{10}$(PGA)-values as a function of magnitude and distance (Fig. 9) by propagating the bootstrap standard deviations of the model parameters (Table 6) into the data domain. At $r > 30$ km and $1.5 < M < 3.5$, the standard deviation is below 0.25 in $\log_{10}(\mathrm{m/s^2})$, whereas for $M = 2.5$ and $r > 30$ km values below 0.1 are determined. As it can be expected from the observed data residuals, the determined standard deviations strongly increase towards the epicenter at $r < 20$ km. However, the bootstrap distribution of the model parameters is slightly skewed (c.f. Figures of the Suplementary Files 1 to 4) and results to an asymmetric distribution of the deviations relative to the original result in the $\log_{10}$(PGA)-domain (Fig. 10). For $M = 3$, there are rather outliers below the original, whereas for $M = 2$ there are rather outliers above the original curve.

Figure 11 shows two examplary distance-decays (rather extreme cases) fitted to PGA-data subsets with earthquakes only from BO and SW respectively.

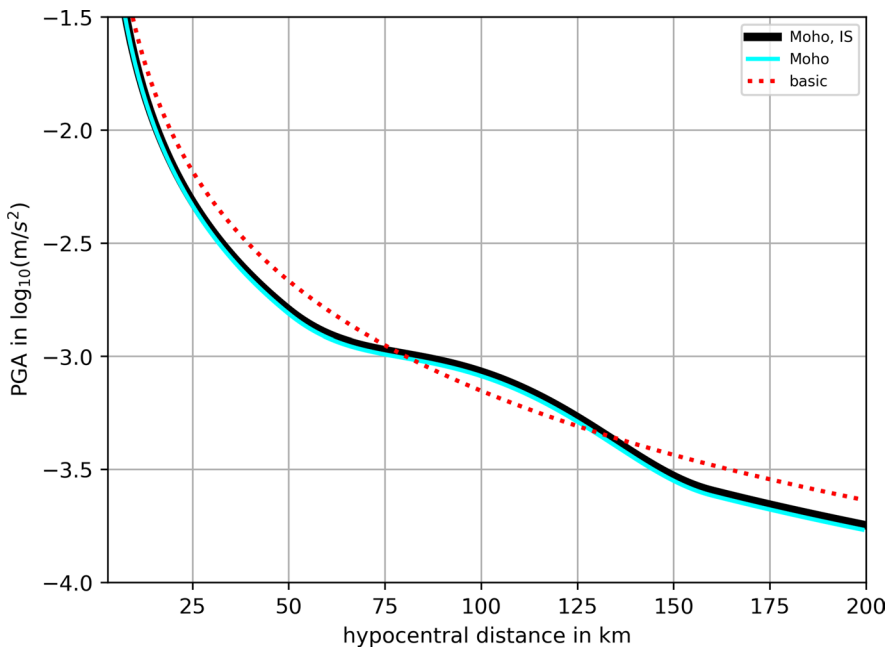

Fig. 7 Optimised median ground motion models

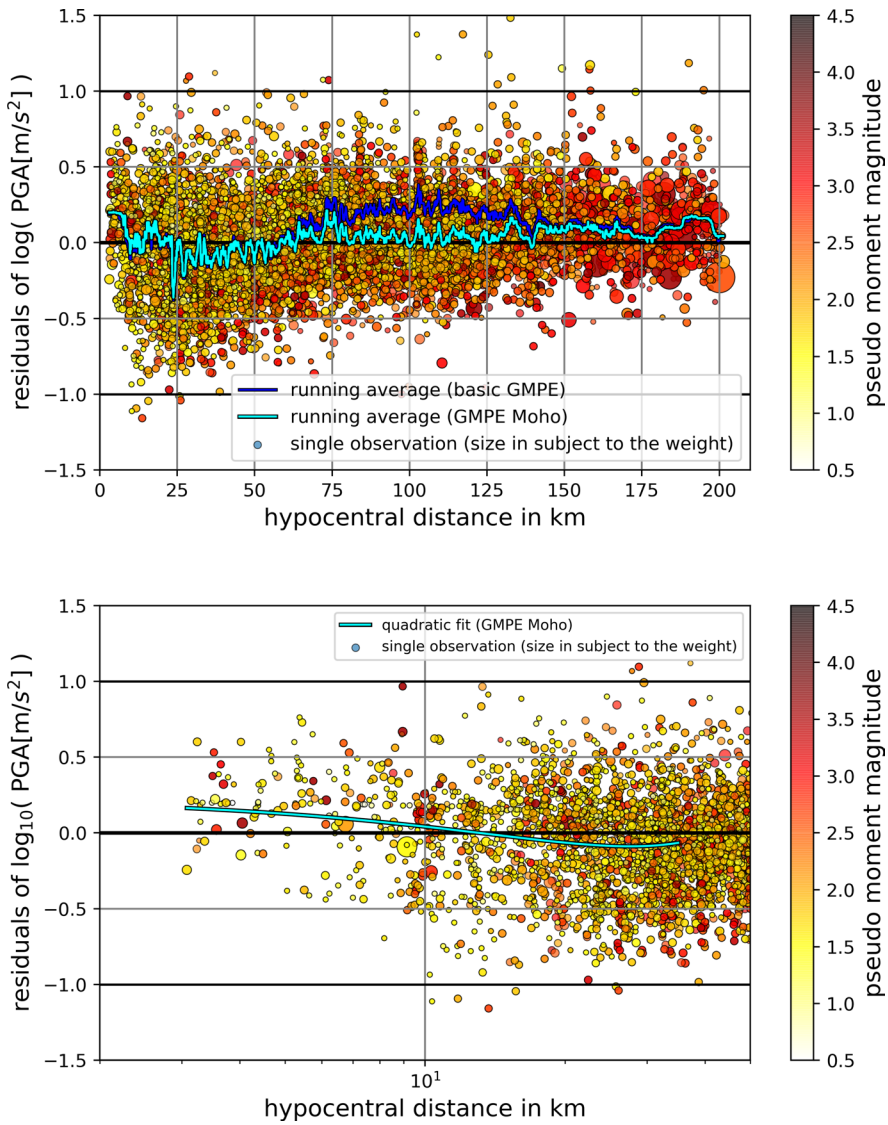

Fig. 8 PGA-residuals between observations and fitted $GMPE^{Moho}$ after applying station corrections and magnitude corrections. Dots represent individual PGA-measures whereby the dot size is a function of the data weight. Top: The cyan (blue) line is the course of the average (moving median with a width of 151 values) in the case of the $GMPE^{Moho}$ ($GMPE^{basic}$). Bottom: The cyan line represents a aquadratic fit of the residuals ($GMPE^{Moho}$) up to 35 km

In the case of BO at around $r \approx 100$ km, the deviations from the median model of the full data set reach the same magnitude (≈ 0.2) as the bootstrap standard deviation of the full data set. In the case of SW, the deviations reach values of about 0.25 at $r > 140$ km. Optimised decays of models from earthquakes at some further regions are shown in the Figure of the Supplementary File 5.

Figure 12 shows the magnitude corrections in dependency of the initial pseudo moment magnitudes. These magnitude corrections can also be understood as removals of between-event residuals. For ground motion predictions, they would reflect the variabilitiy of median ground motions from earthquake to earthquake, if the event magnitudes are determined in accordance with the initial pseudo moment magnitudes of this study.

We observe a slight trend of increasing magnitude corrections with the initial magnitude: corrections of about −0.1 at an initial magnitude of 1.4 to corrections of +0.1 at an initial magnitude of 3.2. Such a trend could be resolved by decreasing the value of coefficient d. Since the regression does not provide a decreased d, it seems that such a decrease of the coefficient also contradicts the PGA data set.

The trend might reflect a systematic correction of the initial magnitudes. However, this trend might also arise from deficiencies of the new optimised

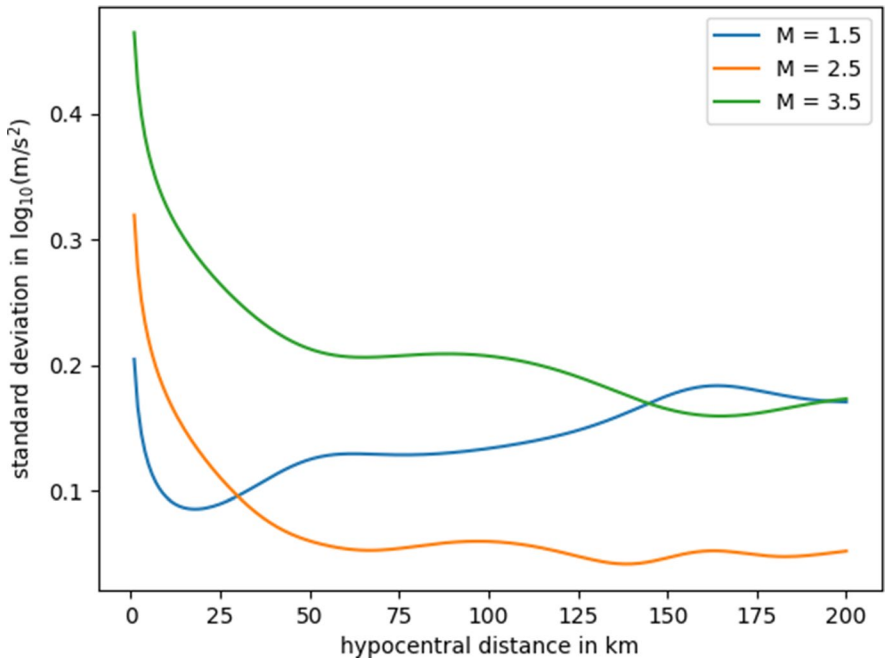

Fig. 9 Bootstrap standard deviation for different magnitudes and in dependency of the hypocentral distance

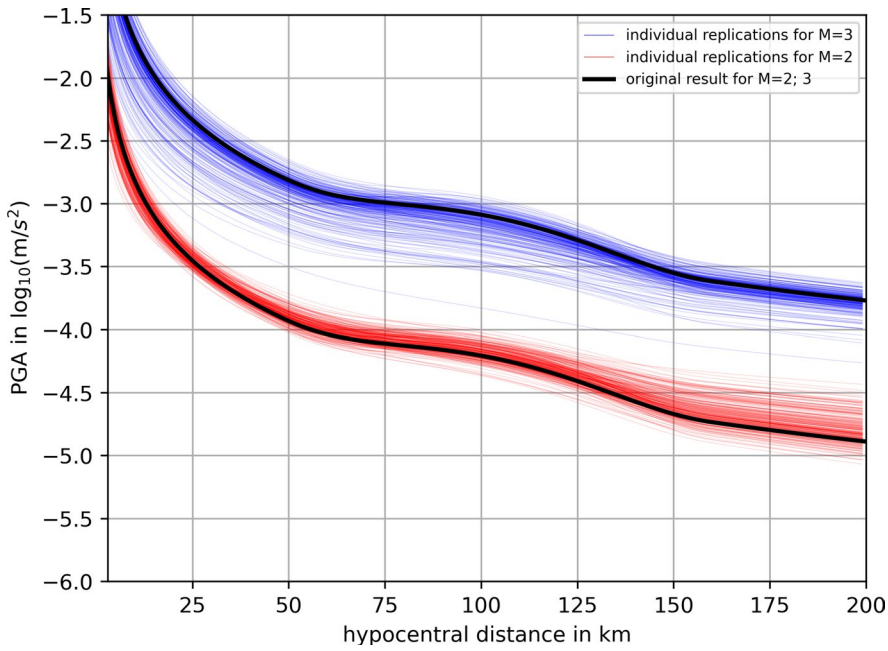

Fig. 10 Distance-decays of individual bootstrap replications (M=2 and M=3 of $GMPE^{Moho}$)

model. These might be shortcomings of the linear magnitude-scaling (see for non-linear scaling, e.g. Munafò et al. 2016), but also remaining deficiencies of the distance-decay might be projected into the magnitude corrections.

5.1.3 Distance-decay at small hypocentral distances

We observe a trend of decreasing PGA-residuals with distance in the range up to 30 km which could not be explained from $GMPE^{Moho}$ (Fig. 8). We aimed for reducing this trend by introducing the

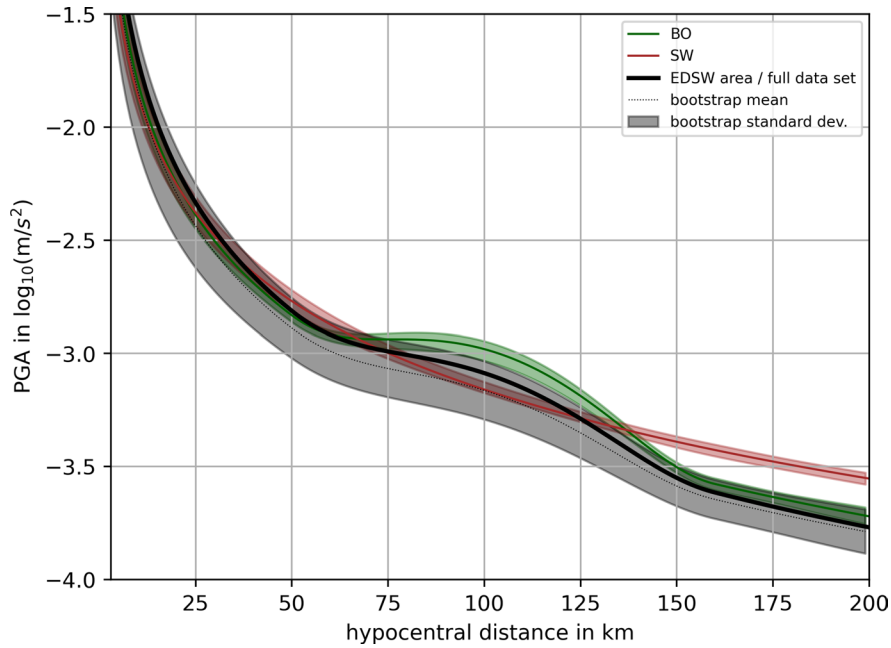

Fig. 11 Median distance-decays ($M = 3$) of $\text{GMPE}^{\text{Moho, IS}}$ optimised to the full data set as well as to selected data with earthquakes at SW and BO. Furthermore, the corresponding bootstrap standard deviations derived from 250 (full data set) and 200 (BO, SW) replications are shown

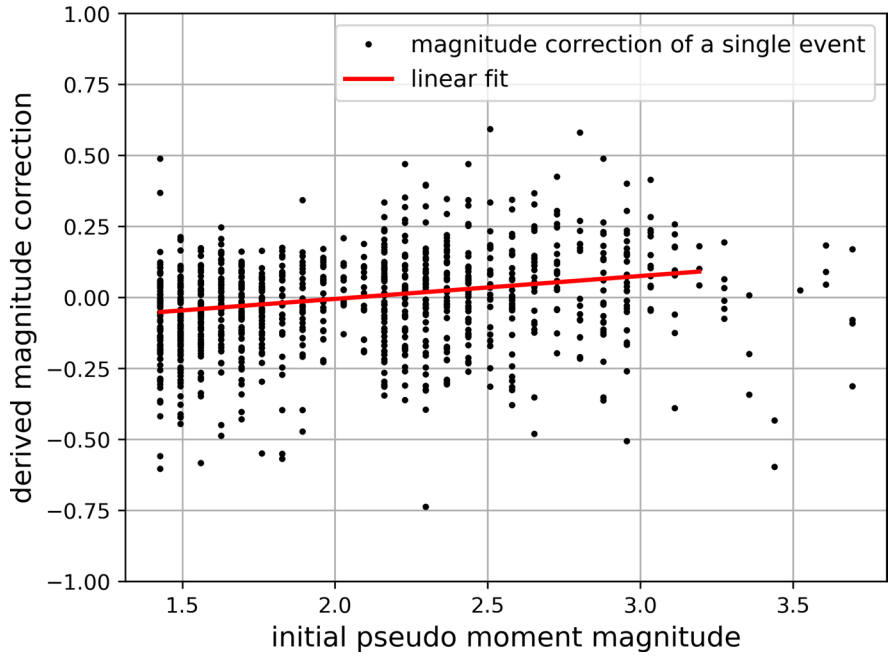

Fig. 12 Optimised magnitude corrections (to $\text{GMPE}^{\text{Moho}}$) in dependence of the initial moment magnitude of individual events

second-order magnitude-dependent distance term $\log_{10}\left(1 + z \cdot 10^{m \cdot M} \cdot r^{p}\right)$. However, this trend is hardly reduced using $\text{GMPE}^{\text{Moho,IS}}$ with $p = -1$ and $m = 0.5$ and the value $z = 0.0054$ is lower than it might be expected. Assuming an S-wave velocity of $\beta = 3.5$ km/s and c' between -1.2 and -2.6 (cf. Section 3.3), z is expected in the range between 0.013 and 0.347.

Further tests with changed values p and m or with regressing p and m partially show increased values of z. But these regressions also do not provide significantly improved data fits or they even show instable behaviours. The trade-offs between the coefficients

seem to be too large to allow a credible determination of them.

5.2 Site responses in geological context

We inspect the station corrections (see Fig. 13 and Table 4) of GMPE^{Moho,IS} in relation to geological units and rock type, and summarise the observed station corrections for groups of station sites. Thereby, we use geological maps and subsurface information from several public authorities and Seismological Services (see Section 9). In the following, we describe the summarised station corrections as listed in Table 3. In the case of specific interests, more details can be found in Appendix A.2.

The derived station corrections to account for site effects indicate known relations between rock types and amplification. The surficial lithology can explain the regional trends of the station corrections at a first order. Rather negative station corrections can be observed towards the Alps (e.g. GF, BY, WF) or at subsurface stations. Moderate corrections are

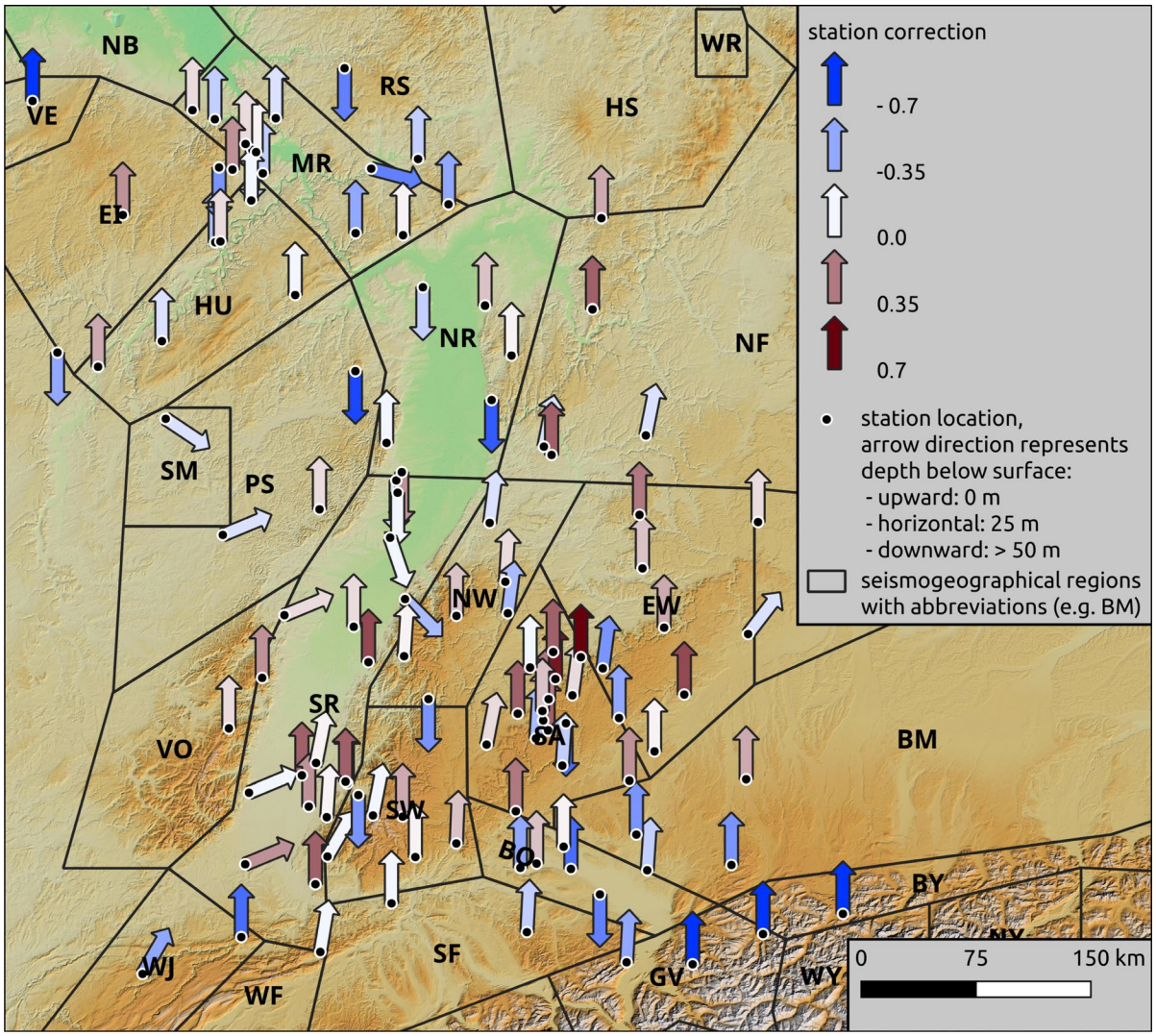

Fig. 13 Derived station corrections of GMPE^{Moho,IS}. The arrow direction represents the depth of the station below the surface. An upward arrow represents a station at the surface. The rotation angle of the arrow increases with depth of the station until a depth of 50 m (downward arrow). Abbreviations of the seismogeographical regions, as defined by Leydecker (2011), are explained in Table 1

commonly observed on (1) magmatic, metamorphic, and consolidated sedimentary rocks of the Black forest; on (2) Jurassic limestones of the Swabian Jura and Eastern Württemberg (SA, EW); and on (3) Devonian clay- and siltsones of the central area of the Rhenish Massif. Positive station corrections are present on the Quarternary sediments within the Upper Rhine Graben of SR and NR, and on the Quarternary sediments of the Swabian Jura and Eastern Württemberg.

Of particular note is that the stations on the Swabian Jura and Eastern Württemberg show large variabilities which can be explained with the alteration of surficial limestones and the existance of surficial sedimentary layers. Such high variabilities could also exist in other regions, but might be undissolved due to a limited density of the station network. Also within individual station groups, the span widths of the station corrections range from 0.3 to 0.8 indicating that other unconsidered ground motion effects are essential.

The median station corrections of the groups c to f range between −0.11 and 0.16. These groups correspond to the class A of the Eurocode 8 (rock conditions), so that we can confidently define the class A of Eurocode 8 as reference rock of the derived model. Regarding the regulations in Germany where DIN EN 1998-1/NA:2021-07 is applied, the reference of the GMPE corresponds to foundation ground class (Baugrundklasse) A combined with the geological underground class (geologische Untergrundklasse) R.

6 Comparison with available ground motion models

We compare the deduced model $\text{GMPE}^{\text{Moho,IS}}$ with ground motion models by Boore et al. (2014); Atkinson (2015) and Bindi et al. (2017). The comparison models are based on subsets of the NGA-West2 database (Ancheta et al. 2014) which comprises global data from active crustal regions.

Boore et al. (2014) applies a sophisticated functional form that considers many ground motion effects and is derived from earthquakes with $3 \leq M_{\text{W}} \leq 7.9$. The model by Bindi et al. (2017) is specifically designed for hazard assessments in areas with low-to-moderate seismic activity. They apply a simpler functional form, but still consider most important motion effects as magnitude-dependent distance-decay, saturation of magnitude-scaling, and site effects that

Table 3 Station groups with the median, standard deviation σ_{g}, minimum, and maximum of the station corrections s_s in $\log_{10}(\text{m}/s^2)$ for each group (DEP12 is not counted, since it is replaced by GLOK at the same location)

Group	Group description	Median	σ_{g}	Min.	Max.
a	Northern Limestone Alps DAVA, RETA, OBER	−0.66	–	−0.65	−0.70
b	Molasse rocks or Quarternary layer above molasse rocks of BO A103D, UBR, TETT, KONZ, STEIN, SISB, WALHA	−0.32	0.23	−0.51	0.13
c	Jurassic limestone of SA and EW MSS, ERPF, BHBD, GUT, BUCH, ZWI, HDH, DEGG	−0.11	0.22	−0.33	0.24
d	Devonian clay-and siltstone of Rhenish Massif AHRW, BEUR, DEP08, RIVT, ABH, FSH, GWBD, OCHT, GWBC, GLOK (DEP12), DEP14, TDN, TNS, BHE	−0.07	0.18	−0.32	0.31
e	Magmatic, metamorphic on URG shoulders WBA, WBB, KTD, ECH, PEB, VOEL, METMA, ENDD, FELD, BERGE, OPP	0.03	0.10	−0.10	0.22
f	Triassic consolidated sedimentary rocks on URG shoulders LBG, BRET, GALG, A124A, SLE, WBG, FLIN, MILB, A115A	0.16	0.22	−0.22	0.42
g	unconsolidated sediments above Tertiary rocks in URG basin FBB, A123A, WLS, BREM, LOES, BREI, OFFE, FREI, STAU	0.31	0.18	0.03	0.51
h	unconsolidated sediments (thickness > 10 m) of SA and EW JUNG, BALG, SAUL, EBIN, TUEB, MSGN, REUL, A108A	0.43	0.14	0.30	0.73

correlate with near-surface rocks/S-wave velocities v_{S30}. The model by Atkinson (2015) is rather suited to very shallow or induced seismicity with $3 \leq M_W \leq 6$ and focuses on ground motion at hypocentral distances less than 40 km.

The distance-decays of the models are shown in Fig. 14 for $M_W = 3$, $v_{S30} = 1000$ m/s, and for PGA-values from maximum rotated horizontal components. Therefore, adjustments from Boore and Kishida (2016) are applied to achieve PGA-values from maximum rotated horizontal components, and the site response model from Boore et al. (2014) is applied on the model from Atkinson (2015). Whereas the models by Atkinson (2015) and Bindi et al. (2017) show the ground motion from unspecified focal mechanisms, a strike-slip mechanism is selected for the model by Boore et al. (2014). The model by Boore et al. (2014) is shown for two cases of attenuation: moderate apparent anelastic attenuation (California, New Zealand, and Taiwan) and low apparent anelastic attenuation (China and Turkey).

$GMPE^{Moho,IS}$ predicts higher PGA at $r > 70$ km. High predictions of $GMPE^{Moho,IS}$ in the range from about 70 to about 150 km are comprehensible due to the incorporation of the term $f_{Moho}(r)$. At $r < 70$ km, both the model $GMPE^{Moho}$ and the model $GMPE^{Moho,IS}$ most widely resemble the median decays of the comparison models. For distances from 4 to 40 km, the differences between the prediction of $GMPE^{Moho,IS}$ and the model by Atkinson (2015) are in the range between about −0.1 and +0.1 (in $\log_{10}$ -space). Although the use of the second-order geometrical decay has not resulted in a remarkably steeper decay at the very close distances, we see that $GMPE^{Moho,IS}$ still approximates the model by Atkinson (2015) at the very small distances.

Relatively high PGA are observed in the case of $GMPE^{Moho,IS}$ at distances $r > 160$ km. This might be due to an actual low anelastic attenuation in the study area — lower than for the areas of China and Turkey. Also, the studies by Kotha et al. (2020, 2022) indicate lower attenuation (at 10 Hz) for the Northern Alps and for the URG (the northwesetern end of their study area) than for Turkey. However, low attenuation might also be pretended by a wider impact of the reflection phases that is not covered by $f_{Moho}(r)$, or by inconsistencies of the determined magnitudes (cf. Section 5.1.2).

Figure 15 shows the predicted PGA-values for the different models as a function of magnitude at a hypocentral distance of 40 km. The slope of $GMPE^{Moho,IS}$ seems to be quite reasonable as an extension of the comparison models towards lower magnitudes. Nevertheless, we recognise a larger slope of $GMPE^{Moho,IS}$ together with rather large PGA-values at magnitudes $M_W > 3.5$. This suggests that an extrapolation of $GMPE^{Moho,IS}$ is doubtful. At a magnitude of 5, $GMPE^{Moho,IS}$ predicts PGA-values which are about 3 times larger (+0.5 in $\log_{10}$-space) than the comparison models.

7 Discussion

7.1 Median ground motion model

We fitted GMPEs to observed peak ground acceleration (PGA) using the earthquake catalogue and the recordings of the EDSW. The initially applied functional form considers first-order geometrical spreading, linear magnitude-scaling, and apparent anelastic attenuation. For that, the PGA-values were extracted in an automatic process and weights are used during the fitting process to balance impacts of different hypocentral distances, magnitude ranges, and the different seismogeographical regions. The composition of the data set was not declustered regarding earthquake similarities (due to similar locations and source mechanisms or due to similarities of main, fore-, and aftershock). The use of respective selection conditions might enhance the quantification of the motion effects in future developments. However, we deduce the following aspects regarding the derived median ground motion model:

(1) The incorporation of the heuristically defined term $f_{Moho}(r)$ to consider wavefield contributions reflected from the Mohorovičić discontinuity results in more uniform distributed median residuals with respect to the hypocentral distance. The scale of impact of the reflections on the observed PGA-values appears be comparable to the scale of impact from varying lithologic conditions of the near-surface. However, tests with data subsets show that also the impact of the reflections depends essentially on the region (Section 5.1.2).

The distance-decay of $GMPE^{Moho,IS}$ deviates from models by Boore et al. (2014) and Bindi et al. (2017)

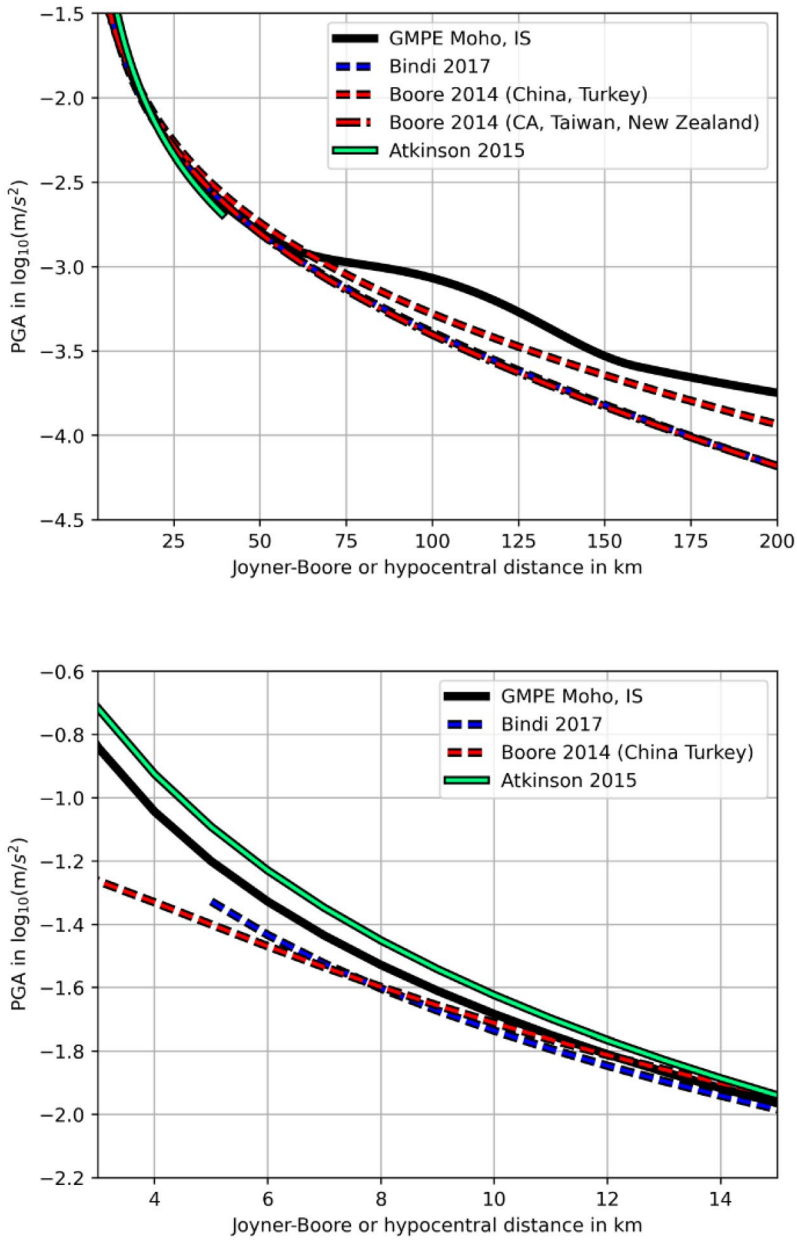

Fig. 14 Top: $\text{GMPE}^{\text{Moho,IS}}$ in comparison with models by Boore et al. (2014); Bindi et al. (2017) and Atkinson (2015) for $v_{S30} = 1000$ m/s, $M_W = 3$ and for PGA-values from maximum rotated horizontal components. The models are shown as a function of hypocentral distance with exception of the model by Boore et al. (2014) which is in dependence of Joyner-Boore distance. More settings and adjustments are described in Section 6. Bottom: close-up for hypocentral distances up to 15 km

whereby the introduced term $f_{\text{Moho}}(r)$ plays an essential role. We believe that the ground motion of the study area might be more influenced from wavefield contributions reflected from the Mohorovičić discontinuity than the areas of the comparison models. We conclude that before applying a ground motion model, the target area needs to be examined regarding the impact of Mohorovičić reflections, and that the models should account for the energy reflected from Mohorovičić discontinuity as the circumstances require. This may also be substantial for hazard assessments, since observations by Bragato et al. (2011) from intensity measures at the Po plain (Northern Italy) suggest that the Mohorovičić discontinuity effect also applies to earthquakes with $M_L > 5.5$.

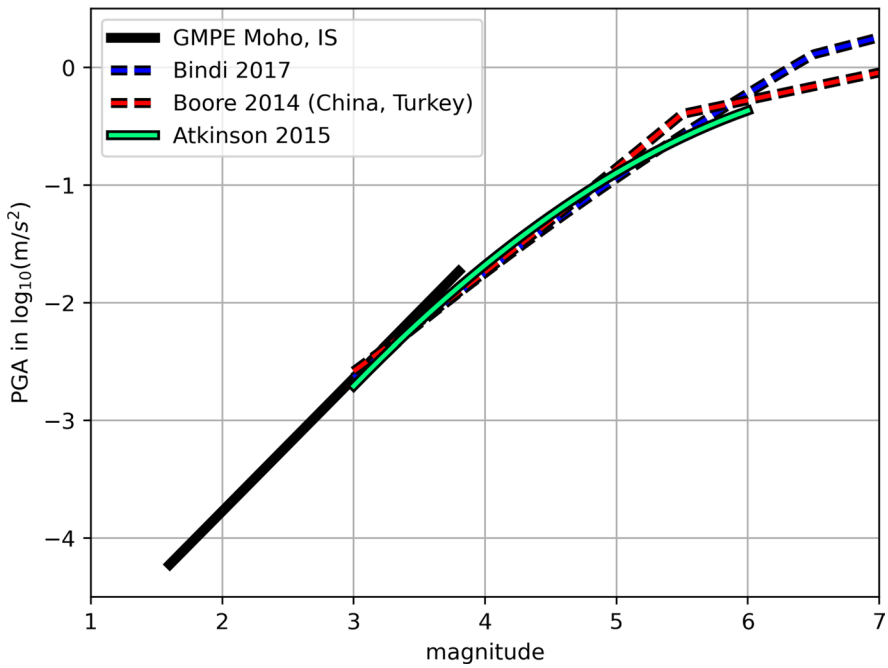

Fig. 15 Magnitude scaling of $\text{GMPE}^{\text{Moho,IS}}$ in comparison with models by Boore et al. (2014); Bindi et al. (2017) and Atkinson (2015) for $v_{S30} = 1000$ m/s, $M_W = 3$ and for PGA-values from maximum rotated horizontal components

In future derivations of ground motion models, a scaling of the effect (coefficient g) depending on source and site region is conceivable. It would be useful to establish clear correlations between g and seismological variables such as source depth, style of faulting, or variables of the Mohorovičić discontinuity (depth, dip, velocity contrast). At the moment, based on the 6 g-values from various subregion data sets, it is difficult to derive meaningful correlations. Another possible modification of the model is an adjustment of the coefficients r_{min} and r_{max} (Eq. 10) according to typical distance ranges where the reflections occur. Assuming that the source depth and the depth of the Mohorovičić discontinuity mainly control the range of the reflection occurances, it could be advantageous to make r_{min} and r_{max} dependent on the local seismogenic depth and the depth of the Mohorovičić discontinuity. Maybe, by introducing such dependencies, the coefficient g would get less region dependent.

(2) Based on theoretical considerations of a general moment-tensor source, a magnitude-dependent second-order geometrical spreading term $f_{geom}(r, M)$ (Eq. 11) is introduced. The scope was to reduce the trend of decreasing PGA-residuals with distance in the range up to 30 km, which could not be explained from $\text{GMPE}^{\text{Moho}}$. However, the trend is hardly reduced using $\text{GMPE}^{\text{Moho,IS}}$. This might come from the approximations of Eq. 11 with fixed values p and m, or from too small weights of the data points which are influenced by the assumed second-order decay. Consequently, modelling of the second-order geometrical spreading effect is prevented although the effect might exist. However, it is also possible that the data set deceives a near-source effect in the PGA-distance relation and the assumed effect actually is negligible.

Looking at the data composition, we see that the PGA-values with $r < 10$ km and from events with $M > 2.5$ are almost exclusively from earthquakes at SA and BO. Near-source records from events with $M > 2.5$ at other regions are lacking. A more sophisticated data set seems to be neccessary to resolve the particularities of the PGA-decay at very small distances and might allow a stable optimisation for z, p, and m. We believe a more appropriate data set to study the near-source behaviour contains ground motion measures of direct phases, whereas other measures from other phases (like Mohorovičić reflections) are excluded. To gather near-source measures, it might be helpful to pursue the seismicity at the geothermal power plants of the region. However, it is likely necessary to complement the regional data with global data to achieve a balanced data distribution with respect to magnitude, distance, and source depth.

(3) Due to local ground motion particularities and possible interaction between magnitude-scaling

and distance-decay, we cannot decide whether the derived ground motion model is directly applicable to other regions, although the comparison with other models implies reasonability. Robust methods that determine moment magnitudes independently from peak motion observations are needed to avoid interactions with the distance-decay and to avoid errors from applying empirical magnitude relations. However, by determining local magnitudes as well as pseudo moment magnitudes M_W in consistency with this study, an application of the derived model at the study area makes sense to account for ground motion particularities.

(4) We do not recommend to use the derived model for earthquakes above the upper mangitude limit ($M = 3.7$) of the data due to the following reasons. Figure 9 shows rather high uncertainties at $M = 3.5$ and the derived median model deviates remarkably at $M > 3.8$ from the comparison models (Section 6). The bootstrap analysis shows an asymmetric distribution (c.f. Section 5.1.2) regarding coefficient d. This might indicate unresolved effects which interfere the determination of the coefficient d. Furthermore, as stated in Section 1.2, the assumed linear magnitude-scaling contradicts the observed non-linear magnitude-scaling of other ground motion models for larger earthquakes.

7.2 Site response in the study area

Although the observed trends appear most widely reasonable, an accurate quantification is difficult because the variations within each site group are in the same order as the median differences between the groups. Biases due to varying prevailing source depths, source mechanisms, and source-to-station geology could be essential since the stations of each station group are limited to a narrow area. For a thorough interpretation, these factors need to be further investigated and quantified. Also, differences with respect to the prevailing phases which commonly generate the peak motion at the individual stations might manipulate the observed station corrections. For instance, at one station, the peak motion is rather caused by Mohorovičić reflections, whereas at other stations this is seldom the case. Probably, site characterisations derived from borehole measurements or surface waves analyses (e.g. compare Garofalo et al. 2016a, b) are neccessary to resolve the impact of the near-surface rocks from other effects reliably.

8 Conclusions

The optimised model $\mathrm{GMPE}^{\mathrm{Moho,IS}}$ predicts horizontal PGA from shallow crustal earthquakes with magnitudes of about $1 < M_W < 3.8$ at the study area. The model accounts heuristically for Mohorovičić reflection phases, which appears important depending on the considered region. The inclusion of the second-order distance-decay term is not adjusting the prediction to a steeper near-source decay at $r < 30$ km, although an increased steepness is seemingly suggested by the data. We believe that a more sophisticated data set is needed to investigate near-source effects of shallow earthquakes.

The stations are grouped with respect to the local geological conditions and can be used to estimate expected site amplifications at a first order. The local lithology explains a strong variability of observed corrections within individual seismogeographical regions. Still, the spread of station corrections within each station group indicates other essential, but unconsidered ground motion effects.

To benefit from the findings more comprehensively in context of seismic hazard assessments, further research is needed to extend the applicability of the model to larger magnitude ranges, or to integrate the findings into other available ground motion models. For further developments of the model, we suggest to (1) gather data from near-source records and from events with larger magnitudes (if available), (2) decluster the data regarding similarities of earthquakes, (3) expand the model to spectral accelerations, (4) test a regionalisation of the expression for the Mohorovičić reflection term, and (5) include events with moment magnitudes determined through spectral fitting methods.

9 Data and resources

Information about the seismic activity of the recent years is provided by the the joint seismological services of Baden-Württemberg and Rhineland-Palatinate (Erdbebendienst Südwest, EDSW). Maps of the seismic activity of the recent years are shown on the web pages of Geological Survey of Baden-Württemberg

(Landesamt für Geologie, Rohstoffe und Bergbau Baden-Württemberg, Regierungspräsidium Freiburg 2019, LGRB) and Geological Survey of Rhineland-Palatinate (Landesamt für Geologie und Bergbau Rheinland-Pfalz 2020, LGB).

To derive the GMPE for Southwestern Germany, the source parameters from the catalogue of the EDSW are used. Used stations are listed in Table 4. The waveform data are provided from State Seismological Services of Baden-Württemberg (LED; 2009); State Seismological Services of Rhineland-Palatinate (LER); Swiss Seismological Service (SED; 1983); French Seismological and Geodetic Network (Résif-RLBP; 1995); Hessian Agency for Nature Conservation, Environment and Geology (HLNUG; 2012); AlpArray working group (2015); Karlsruhe Institute of Technology (KIT; cf. Ritter 2017; Ritter et al. 2019); German Federal Institute for Geosciences and Natural Resources (BGR; 1976); Geological Survey of North Rhine-Westphalia (GD NRW; 215); Central Institution for Meteorology and Geodynamics in Austria (ZAMG; 1987); GEOFON Data Centre (GEOFON; 1993); Paris Institute of Earth Physics and School and Observatory for Earth Sciences of Strasbourg (IPGP and EOST; 1982); Department of Earth and Environmental Sciences, Geophysical Observatory, University of Munich (LMU; 2001); Royal Observatory of Belgium (ROB; 1985); and European Center for Geodynamics and Seismology (ECGS; 2013).

Le RLBP is member of Résif-Epos, a national Research Infrastructure (RI) managed by CNRS-Insu. Inscribed on the roadmap of the Ministry of Higher Education, Research and Innovation, the Résif-Epos IR is a consortium of eighteen French research organisations and institutions. Résif-Epos benefits from the support of the Ministry of Ecological and Solidarity Transition — Doi Résif-RLBP : 10.15778/Résif.FR and 10.15778/Résif.RD

Data processing is performed using Python3 (Van Rossum and Drake 2009) with the ObsPy package (Beyreuther et al. 2010) for waveform processing. To adjust the coefficients for the optimised ground motion model, the Trust Region Reflective algorithm by Branch et al. (1999) within the version 1.2.3. of SciPy (Virtanen et al. 2020) is applied.

To gather geological subsurface information at the station sites, the geological maps from LGB (2020), LGRB (2019), HLNUG (2016), GD NRW (2020), Geological Survey of Austria (Geologische Bundesanstalt in Österreich 2013), Bavarian Environment Agency (Bayerisches Landesamt für Umwelt 2020), and Geological and mining research bureau of France (Service géologique national Bureau de Recherches Géologiques et Minières, 2016) are used. Moreover, the Site Characterisation Database of the SED (2015) is used. To retrieve estimated subsurface structures below the stations of Baden-Württemberg and the Upper Rhine Valley, geological 3D subsurface models of the LGRB (2019) and the GeORG project 2019) are used.

Maps of Figs. 1, 2, and 13 are produced using the software QGIS 3.10 (QGIS Development Team 2009) and using Copernicus data and information funded by the European Union - EU-DEM layers.

Acknowledgements We are very grateful to Klaus Lehmann for proofreading the article thoroughly and for his constructive feedback. We thank Joachim Siemund for a short, but fruitful discussion regarding the bootstrap analysis. We are very grateful to the reviewer(s) whose comments helped to improve the manuscript and to clarify some aspects of the content.

Author contribution Jens Zeiß and Stefan Stange designed the concept of this study. Data processing was performed by Jens Zeiß. All authors contributed to the data analysis and interpretation in joint discussions. Jens Zeiß wrote the first draft and refined the manuscript considering recommendations by Stefan Stange and Andrea Brüstle.

Data Availability Waveform data availability depends on the individual restrictions of the different operators. Extracted PGA-values, the dates and locations of the used earthquakes as well as the used stations are listed in csv-files of the Online Resource.

Code availability The code used for the optimisation procedure is available from the corresponding author on reasonable request.

Declarations

Ethics approval Not applicable

Consent to participate Not applicable

Consent for publication Not applicable

Conflict of interest The authors declare no competing interests.

Appendix A

A.1 List of stations and operators

Table 4 Stations used in this study, the corresponding operators or related project (abbreviations stated in Section 9), locations (WGS-84 coordinates in decimal degree and affiliations to seismogeographical regions), number N_{obs} of the used PGA-values at each station, the determined station corrections s_s for $GMPE^{Moho,IS}$, and the standard deviation σ_s (in $\log_{10}(m/s^2)$) of the observed log(PGA)-values for each station

Station	Operator	Lat.	Lon.	Region	N_{obs}	s_s	σ_s
A100A	AlpArray	48.453	8.926	SA	166	−0.02	0.19
A103D	AlpArray	47.801	9.550	BM	46	−0.35	0.44
A104C	AlpArray	48.127	9.657	EW	48	0.02	0.48
A107D	AlpArray	48.018	10.194	BM	28	0.25	0.38
A108A	AlpArray	48.348	9.831	EW	40	0.47	0.33
A115A	AlpArray	49.274	9.052	NF	24	0.39	0.68
A117A	AlpArray	49.044	9.568	EW	58	0.32	0.33
A123A	AlpArray	48.612	7.891	SR	76	0.11	0.41
A124A	AlpArray	48.654	8.494	NW	120	0.17	0.20
ABH	LER	49.882	7.548	HU	397	−0.06	0.19
AHRW	LER (now: BGR)	50.541	7.076	MR	118	−0.17	0.32
BABA	LED	48.719	8.192	SR	531	−0.22	0.29
BALG	LED	48.273	8.854	SA	53	0.38	0.25
BALST	SED	47.336	7.695	WF	256	0.00	0.22
BERGE	SED	47.872	8.178	SW	498	0.22	0.18
BEUR	LER	50.080	7.078	HU	90	−0.23	0.20
BFO	KIT	48.330	8.330	NW	724	−0.38	0.20
BHBD	LED	48.247	9.003	SA	66	0.18	0.19
BHE	GD NRW	50.353	7.180	EI	92	0.31	0.27
BIW	LER	50.731	7.837	RS	183	−0.44	0.19
BODE	LER & HLNUG	49.911	8.297	NR	91	−0.19	0.27
BOURR	SED	47.395	7.231	WJ	142	−0.47	0.32
BREI	LED	48.033	7.587	SR	47	0.42	0.29
BREM	LED	47.911	7.627	SR	93	0.31	0.30
BRET	LED	49.013	8.689	NW	221	−0.10	0.24
BUCH	LED	48.450	9.353	EW	658	−0.33	0.26
CHMF	Résif-RLBP	47.248	6.652	WJ	124	−0.16	0.19
DAVA	ZAMG	47.287	9.880	GV	64	−0.70	0.20
DEP02	KIT	50.418	7.318	MR	22	0.06	0.18
DEP08	KIT	50.237	7.290	HU	52	−0.03	0.24
DEP12	KIT	50.545	7.430	MR	16	−0.08	0.12
DEP14	KIT	50.449	7.256	MR	42	0.12	0.18
DEGG	LED	48.608	9.713	EW	259	0.24	0.23
DUP	LER	49.412	6.788	SM	28	−0.10	0.12
EBIN	LED	48.208	9.032	SA	37	0.41	0.28
ECH	Résif-RLBP	48.216	7.158	VO	386	0.12	0.24
EMING	SED	47.893	8.843	SA	298	0.35	0.32
ENDD	LED	47.714	7.737	SW	522	−0.05	0.34
ERPF	LED	48.345	9.175	SA	43	0.10	0.20
FACH	LER	50.356	7.994	MR	238	−0.39	0.28
FBB	LED	48.002	7.853	SR	125	0.06	0.22
FELD	LED	47.876	8.004	SW	588	−0.05	0.32

Table 4 (continued)

Station	Operator	Lat.	Lon.	Region	N_{obs}	s_s	σ_s
FLIN	LED	49.306	9.007	NF	27	−0.07	0.27
FREI	LED	48.009	7.843	SR	38	0.39	0.23
FREU	LED	48.236	9.137	SA	455	−0.49	0.28
FSH	LER	50.083	7.109	HU	23	0.10	0.24
GALG	LED	48.786	8.781	NW	441	0.10	0.21
GLOK	LER	50.545	7.434	MR	94	0.06	0.21
GUT	LED	48.071	9.115	SA	984	−0.13	0.25
GWBC	HLNUG	50.393	8.269	RS	84	−0.16	0.24
GWBD	HLNUG	50.114	7.902	MR	148	−0.28	0.46
GWBE	HLNUG	50.106	8.181	MR	120	0.01	0.37
HDH	LED	48.583	10.206	EW	197	−0.08	0.23
HOHE	Résif-RLBP	48.657	7.484	SR	228	0.12	0.50
ILLF	Résif-RLBP	47.684	7.254	SR	66	0.28	0.38
IMS	LER	49.594	7.901	PS	245	−0.60	0.22
JUNG	LED	48.330	9.035	SA	66	0.37	0.23
KIZ	LED	47.956	7.918	SW	1191	−0.34	0.28
KONZ	LED	47.665	9.166	BO	29	−0.51	0.33
KTD	LER	49.320	8.084	NR	36	−0.02	0.29
LAGB	LER	50.361	7.101	EI	223	−0.36	0.22
LBG	LED	48.664	8.796	NW	279	−0.22	0.17
LDE	LER	49.177	8.141	SR	80	−0.08	0.32
LDO	LER	49.208	8.173	NR	16	0.31	0.48
LIENZ	SED	47.295	9.493	GV	62	−0.28	0.37
LOES	LED	47.605	7.666	SR	43	0.44	0.29
LOH	GD NRW	50.183	6.536	EI	16	0.31	0.49
MEM	ROB	50.609	6.006	VE	38	−0.69	0.22
METMA	SED	47.712	8.253	SW	358	0.00	0.22
MILB	BGR	49.829	9.293	NF	36	0.42	0.18
MSGN	LED	48.408	9.075	SA	24	0.61	0.15
MSS	LED	48.177	8.961	SA	328	−0.22	0.32
NEEW	Résif-RLBP	48.956	8.105	SR	76	0.00	0.45
NICK	LER	50.426	7.296	MR	66	−0.17	0.30
OBER	LMU	47.407	10.293	GV	16	−0.65	0.50
OCHT	LER	50.339	7.358	MR	201	−0.17	0.35
OFFE	LED	48.474	7.978	SR	51	0.51	0.32
ONST	LED	48.283	8.999	SA	32	0.13	0.15
OPP	LED	48.497	8.187	NW	688	0.05	0.21
PEB	LER	49.065	7.690	PS	355	0.12	0.22
RETA	ZAMG	47.487	10.762	BY	14	−0.66	0.26
REUL	LED	48.493	9.224	SA	24	0.73	0.27
RIVT	LER	49.708	6.765	HU	256	−0.09	0.16
ROMAN	SED	47.564	9.336	BO	88	−0.39	0.39
ROTE	LED	48.153	8.671	SA	208	0.09	0.29
ROTT	LER	49.129	8.149	SR	149	−0.05	0.22
SAUL	LED	48.012	9.509	SA	21	0.30	0.31
SIND	LED	49.349	9.606	NF	433	−0.09	0.21
SISB	LED	47.686	8.964	BO	216	0.13	0.29

Table 4 (continued)

Station	Operator	Lat.	Lon.	Region	N_{obs}	s_s	σ_s
SLE	SED	47.766	8.493	SW	228	0.16	0.37
STAU	LED	47.869	7.733	SR	58	0.03	0.29
STEIN	SED	47.670	8.869	BO	124	−0.32	0.32
SULZ	SED	47.529	8.113	SF	124	−0.02	0.31
SWS	LED	49.484	8.701	NR	168	−0.57	0.17
TDN	GD NRW	50.575	6.945	MR	22	0.11	0.19
TETT	LED	47.660	9.614	BM	78	−0.17	0.36
TNS	BGR	50.223	8.447	MR	120	−0.32	0.18
TUEB	LED	48.514	9.062	SA	16	0.45	0.22
UBR	BGR	47.681	10.108	BM	186	−0.35	0.23
URBA	LED	48.838	9.586	EW	304	0.14	0.32
VOEL	Résif-RLBP	48.967	7.123	PS	94	−0.10	0.38
VOGT	LED	48.081	7.670	SR	191	0.03	0.32
WALHA	SED	47.753	9.123	BO	104	−0.06	0.31
WALT	Résif-RLBP	47.966	7.277	SR	90	0.02	0.41
WBA	HLNUG & LED	49.653	8.817	NR	154	0.03	0.17
WBB	HLNUG	49.842	8.662	NR	36	0.18	0.25
WBG	HLNUG	50.170	9.345	NF	22	0.20	0.16
WILA	SED	47.415	8.908	SF	98	−0.15	0.44
WLF	GEOFON	49.665	6.152	EI	46	−0.31	0.18
WLS	Résif-RLBP	48.413	7.354	SR	186	0.27	0.32
WMG	ECGS	49.611	6.391	HU	30	0.22	0.25
WOER	LED	49.016	10.264	FA	70	0.12	0.23
ZWI	LED	48.256	9.448	EW	47	−0.32	0.23

A.2 Description of optimised station corrections

Following, we describe the optimised staton corrections of $GMPE^{Moho,IS}$ considering geological aspects.

Northern Limestone Alps and the Alpine Foreland The three stations DAVA, RETA, and OBER (in BY and eastern GV; station group a) of the Northern Limestone Alps have strong negative station corrections between about −0.7 and −0.6. Only MEM and several subsurface stations (BFO, FREU, ROMAN, SWS, IMS, LAGB, BIW: −0.4 to −0.6) reach similar negative values. The corrections of the stations A103D, UBR, TETT, KONZ, STEIN, SISB, and WALHA (station group b) in the vicinity of the Lake Constance (BO and western BM) are mostly negative (−0.5 to 0.1). They are typically placed on a Quarternary layer above Tertiary molasse rocks or on molasse rocks.

Swabian Jura and Eastern Württemberg The station corrections of the regions SA and EW vary strongly. Stations MSS, ERPF, BHBD, GUT, BUCH, ZWI, HDH, and DEGG (station group c) which are placed on Jurassic limestone show moderate corrections between −0.3 and 0.2. In contrast, other stations (station group h: JUNG, BALG, SAUL, EBIN, TUEB, MSGN, REUL, A108A) of SA have essentially higher values of 0.3 to 0.7. These stations are placed on unconsolidated sediments (mostly Quarternary) with an estimated thickness of about 10 to 50 m which overlays rocks of mostly Jurassic origin. One exception is A104C with a moderate correction (0.0) although placed on a unconsolidated layer above Triassic consolidated rocks. ONST and EMING have station corrections of about 0.1 and 0.4, for which a thin Quarternary layer is estimated (thickness < 10 m or less). Some stations of SA and EW (A100A, URBA, ROTE) including WOER of FA and SIND of NF are

placed on Triassic rocks and show moderate corrections −0.1 to 0.1 with exception of A117A (0.3).

URG with Eastern and Western Graben Shoulders The surficial stations of the URG (including graben shoulders) mostly have positive corrections ranging from 0.0 to 0.5. Thereby, most of the surficial stations (station group e: WBA, WBB, KTD, ECH, PEB, VOEL, METMA, ENDD, FELD, BERGE, OPP) with relatively small corrections (-0.1 to 0.2) are placed on metamorphic or magmatic rocks of the graben shoulders.

Also, other stations (station group f: LBG, BRET, GALG, A124A in NW; SLE in SW; WBG, FLIN, A115A, MILB in NF) on the graben shoulders mostly have moderate corrections of −0.2 to 0.2 and are situated on different consolidated sedimentary rocks (limestone, siltstone, sandstone) of Triassic origin. However, slightly increased values are observed at A115A (0.4) and MILB (0.4), whereby at A115A a thin surficial layer of clay and silt is suspected.

The remaining surficial stations (station group g: FBB, A123A, WLS, BREM, LOES, BREI, OFFE, FREI, STAU) are placed within the graben and have tendentially larger corrections of about 0.0 to 0.5. These are mostly placed on a layer of Quarternary rocks over Tertiary sediments. VOGT (0.0) is one exception and is located on volcanic rocks of the Kaiserstuhl.

Central area of the Rhenish Massif The stations in MR, HU, EI, and RS are commonly placed on Devonian claystone or siltstone. The station corrections of the surface stations on Devonian rock are in the range between −0.3 and 0.3 (station group d: AHRW, BEUR, DEP08, RIVT, ABH, FSH, GWBD, OCHT, GWBC, GLOK/DEP12, DEP14, TDN, TNS, BHE). Other surface stations (GWBE: 0.0, DEP02: 0.1) of MR are placed on different volcanic rocks (meta-igneous or unconsolidated rocks). The two stations WLF (−0.3) and WMG (0.2) are located more apart from the others and are placed on Jurassic respective Triassic rocks. This is in accordance with the corrections of the stations on Jurassic and Triassic rocks in the regions of SA, EW, and FA.

Subsurface stations The subsurface stations commonly show clear negative station corrections. The subsurface stations (FACH, NICK, LAGB, BIW) in the central area of the Rhenish Massif, FREU in SA, BFO in NW, KIZ in SW, IMS in PS, and ROMAN in BO are in the range from −0.2 to −0.6. Still, the subsurface stations within SR and NR (SWS, BODE, BABA, WALT, NEEW, ROTT, LDE, LDO, ILLF, HOHE) show a wide range of corrections between −0.6 and 0.3. We think the existance of more positive corrections compared to subsurface stations at other regions is reasonable since probably not all stations reach the depth of the bedrock.

A.3 Coefficients for subregions

Table 5 Final coefficients of $GMPE^{Moho}$ and the unweighted cost $C_{w_i=1}$ from optimising regional data subsets

Region	a	c	d	g	C with $w_{i=1}$
BO	−1.47	−3.61	1.10	1.00	0.2105
SA	−1.56	−3.47	1.09	1.15	0.2007
NR	−1.43	−3.60	1.07	0.29	0.1637
SW	−1.30	−3.82	1.09	0.01	0.2083
SR	−1.25	−3.96	1.09	0.34	0.1991
MR	−1.42	−3.62	1.07	0.49	0.1893

A.4 Statistics of bootstrap analysis

Table 6 Standard deviation $\sigma_{bootstrap}$ as well as median, 16th and 84th percentile (Q_{50}, Q_{16}, Q_{84}) of the model parameters determined from 250 bootstrap replications for $GMPE^{Moho}$

	a	c	d	g
Bootstrap mean	−1.50	−3.37	1.01	0.51
$\sigma_{bootstrap}$	0.14	0.24	0.16	0.20
Q_{50}	−1.52	−3.40	1.04	0.49
Q_{16}	−1.63	−3.57	0.85	0.31
Q_{84}	−1.33	−3.18	1.14	0.72

A.5 Approximate distance-decay considering the intermediate wavefield

Several authors have reported an increased attenuation slope at small distances for shallow earthquakes (Chang et al. 2001; Cotton et al. 2008; Atkinson 2015). To model this effect, Cotton et al. (2008) recommended to include a term that is dependent on focal depth of the earthquake as done by Chang

et al. (2001). Cotton et al. (2008) further associate the dependency on depth with an effect investigated by Frankel et al. (1990). Frankel et al. (1990) showed that a steep decay proportional to $r^{-1.5}$ between 15 and 90 km can be explained by reflections at the bottom side of the layer interfaces above the sources. For this purpose, they compared a velocity model with two layers above the source with a model without discontinuities above. Without discontinuities above the source, a decay of r^{-1} was observed.

In this study, we observe a steep decay of amplitude residuals within the distance up to 30 km which could not be explained from the decay term $f_{\mathrm{geom}}(r_{e,s}) = a \log_{10}(r_{e,s})$ with the fitted regression coefficients of about $a \approx -1.5$. In the following, we consider the wavefield from a general moment-tensor source in an unbounded medium and allow several simplifications. The approximated near-/intermediate-field terms are used to test, if near-/intermediate-fields can reproduce the increased slope near the source.

A.5.1 Wavefield terms of a general moment-tensor source

The various components of the seismic wavefield from a general moment-tensor source are stated by Lokmer and Bean (2010). First, we rearrange their equation

$$\begin{aligned}\mathbf{\Psi}_{\mathrm{N}} =& \mathbf{R}^{\mathrm{N}}(\theta)\,\frac{M(\omega)}{4\pi\rho\alpha^2 r^2}\left\{\left[\frac{i}{2\pi n_\lambda}-\left(\frac{1}{2\pi n_\lambda}\right)^2\right]\cdot e^{2i\pi n_\lambda}\right.\\ &\left.-\left[\frac{\alpha}{\beta}\frac{i}{2\pi n_\lambda}-\left(\frac{1}{2\pi n_\lambda}\right)^2\right]\cdot e^{2i\frac{\alpha}{\beta}\pi n_\lambda}\right\}\end{aligned} \tag{15}$$

for the near field to

$$\mathbf{\Psi}_{\mathrm{N}} = \mathbf{\Psi}_{\mathrm{N1}} + \mathbf{\Psi}_{\mathrm{N2}} \tag{16}$$

with

$$\mathbf{\Psi}_{\mathrm{N1}} = \mathbf{R}^{\mathrm{N}}(\theta)\,\frac{M(\omega)}{4\pi\rho\alpha^2 r^2}\,\frac{1}{4\pi^2 n_\lambda^2}\left(e^{i2\pi n_\lambda} - e^{i2\frac{\alpha}{\beta}\pi n_\lambda}\right) \tag{17}$$

and

$$\begin{aligned}\mathbf{\Psi}_{\mathrm{N2}} =& \mathbf{R}^{\mathrm{N}}(\theta)\,\frac{M(\omega)}{4\pi\rho\alpha^2 r^2}\,\frac{1}{2\pi n_\lambda}\\ &\cdot\left(e^{i(2\pi n_\lambda+\pi/2)} - \frac{\alpha}{\beta}e^{i\left(2\frac{\alpha}{\beta}\pi n_\lambda+\pi/2\right)}\right).\end{aligned} \tag{18}$$

The corresponding intermediate wavefields $\mathbf{\Psi}_{\mathrm{IP}}$ and $\mathbf{\Psi}_{\mathrm{IS}}$ as well as the far wavefield $\mathbf{\Psi}_{\mathrm{FP}}$ and $\mathbf{\Psi}_{\mathrm{FS}}$ for P- and S-waves read as (Lokmer and Bean 2010)

$$\mathbf{\Psi}_{\mathrm{IP}} = \mathbf{R}^{\mathrm{IP}}(\theta)\,\frac{M(\omega)}{4\pi\rho\alpha^2 r^2}\,e^{i2\pi n_\lambda} \tag{19}$$

$$\mathbf{\Psi}_{\mathrm{IS}} = \mathbf{R}^{\mathrm{IS}}(\theta)\,\frac{M(\omega)}{4\pi\rho\beta^2 r^2}\,e^{i2\frac{\alpha}{\beta}\pi n_\lambda} \tag{20}$$

$$\mathbf{\Psi}_{\mathrm{FP}} = \mathbf{R}^{\mathrm{FP}}(\theta)\,\frac{M(\omega)}{4\pi\rho\alpha^2 r^2}\,2\pi n_\lambda e^{i(2\pi n_\lambda+\pi/2)} \tag{21}$$

$$\mathbf{\Psi}_{\mathrm{FS}} = \mathbf{R}^{\mathrm{FS}}(\theta)\,\frac{M(\omega)}{4\pi\rho\beta^2 r^2}\,2\pi\frac{\alpha}{\beta}n_\lambda e^{i(2\frac{\alpha}{\beta}\pi n_\lambda+\pi/2)} \tag{22}$$

with P- and S-wave velocity α and β, the radiation patterns $\mathbf{R}^{\mathrm{N}}(\theta)$, $\mathbf{R}^{\mathrm{IP}}(\theta)$, $\mathbf{R}^{\mathrm{IS}}(\theta)$, $\mathbf{R}^{\mathrm{FP}}(\theta)$, $\mathbf{R}^{\mathrm{FS}}(\theta)$ of the wavefield parts (near, intermediate P-wavefield, intermediate S-wavefield, far P-wavefield, far S-wavefield), density ρ, the Fourier spectrum $M(\omega)$ of the source depending on angular frequency ω, the distance r to the source, and the distance ($n_\lambda = \frac{r\omega}{2\pi\alpha}$) to the source measured in P-wavelengths.

The dependencies of the wavefield parts on the distance are

$$\mathbf{\Psi}_{\mathrm{N1}} \propto \frac{1}{r^2}\cdot\frac{1}{n_\lambda^2} \tag{23}$$

$$\mathbf{\Psi}_{\mathrm{N2}} \propto \frac{1}{r^2}\cdot\frac{1}{n_\lambda} \tag{24}$$

$$\mathbf{\Psi}_{\mathrm{IP}} \propto \frac{1}{r^2} \tag{25}$$

$$\mathbf{\Psi}_{\mathrm{IS}} \propto \frac{1}{r^2} \tag{26}$$

$$\mathbf{\Psi}_{\mathrm{FP}} \propto \frac{1}{r^2}\cdot n_\lambda \tag{27}$$

$$\mathbf{\Psi}_{\mathrm{FS}} \propto \frac{1}{r^2} \cdot n_\lambda, \tag{28}$$

disregarding the constants of the medium, the source coefficients and the spatial periodicities in Eqs. 17 to 22. We see that the distance-decay of the far (intermediate) P-wavefield behaves as the distance-decay of far (intermediate) S-wavefield. Further on, the intermediate field decay is one order higher than the far field decay with respect to n_λ. The part $\mathbf{\Psi}_{\mathrm{N1}}$ ($\mathbf{\Psi}_{\mathrm{N2}}$) of the near field decay is two (one) order higher than the intermediate fields with repect to n_λ.

A.5.2 Simplifications for an approximated PGA-decay

Since the spatial decay of the far (intermediate) P-wavefield behaves as the far (intermediate) S-wavefield behaviour (Appendix A.5.1), and since PGA on the horizontal components is rather composed by the S-phases than by P-phases, we omit the P-wavefields to derive a simple form for an approximated overall decay. We also neglect the near wavefield, since its order of decay is still higher than the intermediate wavefield decays. It remains the intermediate S-wavefield and the far S-wavefield:

$$\mathbf{\Psi}_{\mathrm{IS}}(\omega) = \mathbf{R}^{\mathrm{IS}}(\theta)\, \frac{M(\omega)}{4\pi\rho\,\beta^2\, r^2}\, e^{i2\frac{\alpha}{\beta}\pi n_\lambda} \tag{29}$$

$$\mathbf{\Psi}_{\mathrm{FS}}(\omega) = \mathbf{R}^{\mathrm{FS}}(\theta)\, \frac{M(\omega)\,\alpha\, n_\lambda}{2\rho\,\beta^3\, r^2}\, e^{i(2\frac{\alpha}{\beta}\pi n_\lambda + \pi/2)}. \tag{30}$$

In the following, we consider the decay of Eqs. 29 and 30 only at the dominant period T_0 of the spectral wavefield so that we can write for the number of wavelengths for the dominant angular frequency ω_0 or dominant period T_0:

$$n_{\lambda 0} = \frac{\omega_0\, r}{2\pi\alpha} = \frac{r}{T_0\,\alpha}\,. \tag{31}$$

We further neglect the azimuthal dependency of the radiation patterns ($\mathbf{R}^{\mathrm{IS}} = \mathbf{R}^{\mathrm{FS}} = 1$), the spatial periodicity ($e^{i(2\frac{\alpha}{\beta}\pi n_\lambda + \pi/2)} = 1$), and introduce the factors $z^{\mathrm{IS}} = \frac{M(\omega)}{4\pi\rho\beta^2}$ and $z^{\mathrm{FS}} = \frac{M(\omega)\,\alpha}{2\rho\beta^3}$. With Eq. 31 and the described simplification, we can write for the considered wavefields (Eqs. 29 and 30):

$$\mathbf{\Psi}_{\mathrm{IS}}\,|_{T=T_0} = z^{\mathrm{IS}} \cdot \frac{1}{r^2} \tag{32}$$

$$\mathbf{\Psi}_{\mathbf{FS}}|_{T=T_0} = \frac{z^{\mathrm{FS}}}{\alpha} \cdot \frac{1}{r \cdot T_0}\cdot \tag{33}$$

Consequently, we can write for their ratio:

$$\left.\frac{\mathbf{\Psi}_{\mathrm{IS}}}{\mathbf{\Psi}_{\mathrm{FS}}}\right|_{T=T_0} = \frac{z^{\mathrm{IS}} \cdot \alpha}{z^{\mathrm{FS}}} \cdot \frac{T_0}{r}. \tag{34}$$

We sum up the wavefields $\mathbf{\Psi}_{\mathrm{FS}}$ and $\mathbf{\Psi}_{\mathrm{IS}}$ and use Eqs. 33 and 34:

$$\begin{aligned} &\mathbf{\Psi}_{FS}|_{T=T_0} \;+\; \mathbf{\Psi}_{IS}|_{T=T_0} \\ &\quad = \mathbf{\Psi}_{FS} \cdot \left(1 + \frac{\mathbf{\Psi}_{IS}}{\mathbf{\Psi}_{FS}}\right)\Bigg|_{T=T_0} \\ &\quad = \frac{z^{FS}}{\alpha} \cdot \frac{1}{T_0} \cdot\; r^{-1} \cdot \left(1 + \frac{\alpha \cdot z^{IS}}{z^{FS}} \cdot T_0 \cdot r^{-1}\right). \end{aligned} \tag{35}$$

On the lines of the summation of the wavefield parts, we test a summation of the PGA parts, consider the logarithmic space, and introduce the exponents a and p to allow deviations from the theoretical decay ($p = -1$ and $a = -1$):

$$\begin{aligned} &\log_{10}\left(\mathrm{PGA}^{\mathrm{FS}} + \mathrm{PGA}^{\mathrm{IS}}\right) \\ &= \log_{10}\left(\frac{z^{\mathrm{FS}}}{\alpha \;\cdot\; T_0} \;\cdot\; r^a \cdot \left(1 + \frac{z^{\mathrm{IS}} \cdot \alpha}{z^{\mathrm{FS}}}\; T_0 \;\cdot\; r^p\right)\right) \\ &= \log_{10}\left(\frac{z^{\mathrm{FS}}}{\alpha \;\cdot\; 10^{m \cdot M + c'}}\right) \;+\; a\, \log_{10}(r) \\ &\quad + \log_{10}\left(1 + \frac{z^{\mathrm{IS}} \cdot \alpha}{z^{\mathrm{FS}}} \cdot 10^{m \cdot M + c'} \;\cdot\; r^p\right). \end{aligned} \tag{36}$$

The expression $10^{m \cdot M + c'}$ estimates the predominant period (in s) from the event magnitude according to empirical scaling relations. Sato (1979) states several empirical relations of predominant period T_0 (in s) with P- and S-waves from studies by Kasahara (1957); Terashima (1968); Furuya (1969), and Yamaguchi et al. (1978). The relations have the form of $\log_{10}(T_0) = m \cdot M + c'$ with a constant c' and a coefficient m that ranges from 0.4 to 0.58 depending on the study.

The transfer from wavefield summation to PGA summation is strictly speaking not valid, since the various wavefield parts do not necessarily superimpose to maximum values. However, we believe that the approach is still useful. The part $\mathrm{PGA}^{\mathrm{IS}}$ of the intermediate S-wavefield vanishes at large hypocentral distances. At small hypocentral distances, the

PGA part of the far field is small in comparison to the near field part. Hence, we expect that Eq. 36 can be used as a first-order approximation including the decay of PGA^{IS}.

We get an alternative definition of the geometrical decay from Eq. 6 by considering the terms of Eq. 36 which are dependent on r and by defining $z = \frac{z^{IS} \cdot \alpha}{z^{FS}} \cdot 10^{c'} = \frac{\beta}{2\pi} \cdot 10^{c'}$ (α and β in km/s):

$$f_{geom}(r, M) = a \log_{10}(r) + \log_{10}\left(1 + z \cdot 10^{m \cdot M} \cdot r^{p}\right). \quad (37)$$

Hereby, the term $a \log_{10}(r)$ corresponds to the geometrical decay of $GMPE^{basic}$. The omitted expression $\log_{10}\left(\frac{z^{FS}}{\alpha \cdot 10^{m \cdot M + c'}}\right) = \log_{10}\left(\frac{z^{FS}}{\alpha}\right) - mM - c'$ of Eq. 36 is independent from r and will be projected into $f_{M(M)} = d \cdot M$ and into the constant c (cf. Eqs. 5 and 8).

The coefficient p controls the steepness of the PGA-decay near the source relative to the far field decay. The coefficients z and m scale the PGA-values in relation to the far field PGA-values. Whereas z is independent from the event magnitude, the product $m \cdot M$ accounts for an amplitude scaling of the intermediate field with magnitude that differs from the scaling of the far field.

References

Abrahamson NA, Silva WJ, Kamai R (2014) Summary of the ASK14 ground motion relation for active crustal regions. Earthq Spectr 30(3):1025–1055. https://doi.org/10.1193/070913EQS198M

Ahorner L (1983) Historical seismicity and present-day microearthquake activity of the Rhenish Massif, Central Europe. In: Fuchs K, von Gehlen K, Mälzer H, Murawski H, Semmel A (eds) Plateau uplift. Springer, Berlin Heidelberg, pp 198–221

AlpArray Seismic Network (2015) AlpArray Seismic Network (AASN) temporary component. https://doi.org/10.12686/ALPARRAY/Z3_2015

Ambraseys NN, Douglas J, Sarma SK, Smit PM (2005) Equations for the estimation of strong ground motions from shallow crustal earthquakes using data from Europe and the Middle East: horizontal peak ground acceleration and spectral acceleration. Bull Earthq Eng 3(1):1–53. https://doi.org/10.1007/s10518-005-0183-0

Ancheta TD, Darragh RB, Stewart JP, Seyhan E, Silva WJ, Chiou BSJ, Wooddell KE, Graves RW, Kottke AR, Boore DM, Kishida T, Donahue JL (2014) NGA-West2 database. Earthq Spectr 30(3):989–1005. https://doi.org/10.1193/070913EQS197M

Atik LA, Abrahamson N, Bommer JJ, Scherbaum F, Cotton F, Kuehn N (2010) The variability of ground-motion prediction models and its components. Seismol Res Lett 81(5):794–801. https://doi.org/10.1785/gssrl.81.5.794

Atkinson GM (2015) Ground-motion prediction equation for small-to-moderate events at short hypocentral distances, with application to induced-seismicity hazards. Bull Seismol Soc Am 105(2A):981–992. https://doi.org/10.1785/0120140142

Bakun WH, Joyner WB (1984) The ML scale in central California. Bull Seismol Soc Am 74(5):1827–1843

Baltay AS, Hanks TC (2014) Understanding the magnitude dependence of PGA and PGV in NGA-West 2 data. Bull Seismol Soc Am 104(6):2851–2865. https://doi.org/10.1785/0120130283

Bayerisches Landesamt für Umwelt (2020) Digitale Geologische Karte von Bayern 1:25.000 (dGK25). https://www.umweltatlas.bayern.de/mapapps/resources/apps/lfu_geologie_ftz/index.html?lang=de &layers=service_geo_vt3 &lod=5. Accessed 24 July 2020

Beyreuther M, Barsch R, Krischer L, Megies T, Behr Y, Wassermann J (2010) ObsPy: a Python toolbox for seismology. Seismol Res Lett 81(3):530–533. https://doi.org/10.1785/gssrl.81.3.530

Bindi D, Massa M, Luzi L, Ameri G, Pacor F, Puglia R, Augliera P (2014) Pan-European ground-motion prediction equations for the average horizontal component of PGA, PGV, and 5%-damped PSA at spectral periods up to 3.0 s using the RESORCE dataset. Bull Earthq Eng 12(1):391–430. https://doi.org/10.1007/s10518-013-9525-5

Bindi D, Cotton F, Kotha SR, Bosse C, Stromeyer D, Grünthal G (2017) Application-driven ground motion prediction equation for seismic hazard assessments in non-cratonic moderate-seismicity areas. J Seismol 21(5):1201–1218

Bommer J, Douglas J, Scherbaum F, Cotton F, Bungum H, Fäh D (2010) On the selection of ground-motion prediction equations for seismic hazard analysis. Seismol Res Letters 81(5):783–793. https://doi.org/10.1785/gssrl.81.5.783

Boore DM (2009) Comparing stochastic point-source and finite-source ground-motion simulations: SMSIM and EXSIM. Bull Seismol Soc Am 99(6):3202–3216. https://doi.org/10.1785/0120090056

Boore DM, Joyner WB (1982) The empirical prediction of ground motion. Bull Seismol Soc Am 72(6B):S43–S60

Boore DM, Kishida T (2016) Relations between some horizontal-component ground-motion intensity measures used in practice. Bull Seismol Soc Am 107(1):334–343. https://doi.org/10.1785/0120160250

Boore DM, Stewart JP, Seyhan E, Atkinson GM (2014) NGA-West2 equations for predicting PGA, PGV, and 5% damped PSA for shallow crustal earthquakes. Earthq Spectr 30(3):1057–1085. https://doi.org/10.1193/070113EQS184M

Bragato PL, Sugan M, Augliera P, Massa M, Vuan A, Saraò A (2011) Moho reflection effects in the Po Plain (Northern Italy) observed from instrumental and intensity data. Bull Seismol Soc Am 101(5):2142–2152. https://doi.org/10.1785/0120100257

Branch MA, Coleman TF, Li Y (1999) A subspace, interior, and conjugate gradient method for large-scale bound-constrained minimization problems. SIAM Journal on Scientific Computing 21(1):1–23. https://doi.org/10.1137/S1064827595289108

Brüstle W, Hock S, Benn N (2015) Makroseismischer atlas Baden-Württemberg, 2nd edn. University Science Books

Burger RW, Somerville PG, Barker JS, Herrmann RB, Helmberger DV (1987) The effect of crustal structure on strong ground motion attenuation relations in eastern North America. Bull Seismol Soc Am 77(2):420–439

Campbell KW, Bozorgnia Y (2014) NGA-West2 ground motion model for the average horizontal components of PGA, PGV, and 5% damped linear acceleration response spectra. Earthq Spectr 30(3):1087–1115. https://doi.org/10.1193/062913EQS175M

Central Institution for Meteorology and Geodynamics in Austria (1987) Austrian seismic network. https://doi.org/10.7914/SN/OE

Chang TY, Cotton F, Angelier J (2001) Seismic attenuation and peak ground acceleration in Taiwan. Bull Seismol Soc Am 91(5):1229–1246. https://doi.org/10.1785/0120000729

Chen YS, Weatherill G, Pagani M, Cotton F (2018) A transparent and data-driven global tectonic regionalization model for seismic hazard assessment. Geophys J Int 213(2):1263–1280. https://doi.org/10.1093/gji/ggy005

Chiou BJ, Youngs RR (2008) An NGA model for the average horizontal component of peak ground motion and response spectra. Earthq Spectr 24(1):173–215. https://doi.org/10.1193/1.2894832

Chiou BSJ, Youngs RR (2014) Update of the Chiou and Youngs NGA model for the average horizontal component of peak ground motion and response spectra. Earthq Spectr 30(3):1117–1153. https://doi.org/10.1193/072813EQS219M

Cotton F, Scherbaum F, Bommer JJ, Bungum H (2006) Criteria for selecting and adjusting ground-motion models for specific target regions: application to Central Europe and rock sites. J Seismol 10(2):137. https://doi.org/10.1007/s10950-005-9006-7

Cotton F, Pousse G, Bonilla F, Scherbaum F (2008) On the discrepancy of recent European ground-motion observations and predictions from empirical models: analysis of KiK-net accelerometric data and point-sources stochastic simulations. Bull Seismol Soc Am 98(5):2244–2261. https://doi.org/10.1785/0120060084

Deichmann N (2017) Theoretical basis for the observed break in ML/Mw scaling between small and large earthquakes. Bull Seismol Soc Am 107(2):505–520. https://doi.org/10.1785/0120160318

Department of Earth and Environmental Sciences, Geophysical Observatory, University of Munich (2001) BayernNetz. https://doi.org/10.7914/SN/BW

DIN EN 1998-1/NA:2021-07 (2021) National Annex - Nationally determined parameters - Eurocode 8: design of structures for earthquake resistance - part 1: general rules, seismic actions and rules for buildings. https://doi.org/10.31030/3262205

Douglas J (2003) A note on the use of strong-motion data from small magnitude earthquakes for empirical ground motion estimation. In: Skopje Earthquake 40 Years of European earthquake engineering, Skopje https://strathprints.strath.ac.uk/69182/

Douglas J, Edwards B (2016) Recent and future developments in earthquake ground motion estimation. Earth-Science Reviews 160:203–219. https://doi.org/10.1016/j.earscirev.2016.07.005

Douglas J, Jousset P (2011) Modeling the difference in ground-motion magnitude-scaling in small and large earthquakes. Seismol Res Lett 82(4):504–508. https://doi.org/10.1785/gssrl.82.4.504

Edwards B, Allmann B, Fäh D, Clinton J (2010) Automatic computation of moment magnitudes for small earthquakes and the scaling of local to moment magnitude. Geophys J Int 183(1):407–420. https://doi.org/10.1111/j.1365-246X.2010.04743.x

Efron B, Gong G (1983) A leisurely look at the bootstrap, the Jackknife, and cross-validation. The American Statistician 37(1):36–48. https://doi.org/10.2307/2685844

European Center for Geodynamics and Sesimology (ECGS) (2013) Luxembourg seismic network. https://www.fdsn.org/networks/detail/LU/

Fäh D, Gisler M, Jaggi B, Kästli P, Lutz T, Masciadri V, Matt C, Mayer-Rosa D, Rippmann D, Schwarz-Zanetti G, Tauber J, Wenk T (2009) The 1356 Basel earthquake: an interdisciplinary revision. Geophys J Int 178(1):351–374. https://doi.org/10.1111/j.1365-246X.2009.04130.x

Federal Institute for Geosciences and Natural Resources (1976) German Regional Seismic Network (GRSN). https://doi.org/10.25928/MBX6-HR74

Frankel A, McGarr A, Bicknell J, Mori J, Seeber L, Cranswick E (1990) Attenuation of high-frequency shear waves in the crust: measurements from New York State, South Africa, and Southern California. J Geophys Res Solid Earth 95(B11):17441–17457. https://doi.org/10.1029/JB095iB11p17441

Furuya I (1969) Predominant period and magnitude. Journal of Physics of the Earth 17(2):119–126. https://doi.org/10.4294/jpe1952.17.119

Garofalo F, Foti S, Hollender F, Bard P, Cornou C, Cox B, Dechamp A, Ohrnberger M, Perron V, Sicilia D, Teague D, Vergniault C (2016) InterPACIFIC project: comparison of invasive and non-invasive methods for seismic site characterization. Part II: inter-comparison between surface-wave and borehole methods. Soil Dynamics and Earthquake Engineering 82:241–254. https://doi.org/10.1016/j.soildyn.2015.12.009

Garofalo F, Foti S, Hollender F, Bard P, Cornou C, Cox B, Ohrnberger M, Sicilia D, Asten M, Di Giulio G, Forbriger T, Guillier B, Hayashi K, Martin A, Matsushima S, Mercerat D, Poggi V, Yamanaka H (2016) InterPACIFIC project: comparison of invasive and non-invasive methods for seismic site characterization. Part I: intra-comparison of surface wave methods-. Soil Dyn Earthq Eng 82:222–240. https://doi.org/10.1016/j.soildyn.2015.12.010

GEOFON Data Centre (1993) GEOFON Seismic Network. https://doi.org/10.14470/TR560404

Geological Survey of North Rhine - Westphalia (GD NRW) (2015) Geological survey of North Rhine - Westphalia (GD NRW). https://www.fdsn.org/networks/detail/NH/

Geologische Bundesanstalt in Österreich (2013) Kartographisches Modell 1:500.000 Austria - Geologie. https://gisgba.geologie.ac.at/gbaviewer/?url=https://gisgba.g eologie.ac.at/arcgis/rest/services/KM500/AT_GBA_KM500_AUSTRIA_ GE/MapServer. Accessed 30 Oct 2020

Geologischer Dienst Nordrhein-Westfalen (2020) Informationssystem Geologische Karte von Nordrhein-Westfalen 1:100.000 - WMS. http://www.wms.nrw.de/gd/GK100?VERSION=1.3.0 &SERVICE=WMS &REQUEST=GetCapabilities. Accessed 24 July 2020

GeORG project team (2019) LGRB-Kartenviewer. http://maps.geopotenziale.eu/. Accessed 30 Oct 2020

Grünthal G, Stromeyer D (1992) The recent crustal stress field in central Europe: trajectories and finite element modeling. J Geophys Res Solid Earth 97(B8):11805–11820. https://doi.org/10.1029/91JB01963

Häring MO, Schanz U, Ladner F, Dyer BC (2008) Characterisation of the Basel 1 enhanced geothermal system. Geothermics 37(5):469–495. https://doi.org/10.1016/j.geothermics.2008.06.002

Heidbach O, Reinecker J, Tingay M, Müller B, Sperner B, Fuchs K, Wenzel F (2007) Plate boundary forces are not enough: second- and third-order stress patterns highlighted in the World Stress Map database. Tectonics 26(6):6014. https://doi.org/10.1029/2007TC002133

Hensch M, Dahm T, Ritter J, Heimann S, Schmidt B, Stange S, Lehmann K (2019) Deep low-frequency earthquakes reveal ongoing magmatic recharge beneath Laacher See Volcano (Eifel, Germany). Geophys J Int 216(3):2025–2036. https://doi.org/10.1093/gji/ggy532

Hessian Agency for Nature Conservation, Environment and Geology (2012) Hessischer Erdbebendienst. https://doi.org/10.7914/SN/HS

Hessisches Landesamt für Naturschutz, Umwelt und Geologie (HLNUG) (2016) Geologische Übersichtskarte 1:300000 (Version 2.0 M. Hoffmann). http://geologie.hessen.de/mapapps/resources/apps/geologie/ind ex.html?lang=de. Accessed 10 Oct 2020

Hinzen KG (2003) Stress field in the Northern Rhine area, Central Europe, from earthquake fault plane solutions. Tectonophysics 377(3):325–356. https://doi.org/10.1016/j.tecto.2003.10.004

Kasahara K (1957) The nature of seismic origins as inferred from seismological and geodetic observations. Bull Earthq Res Inst 35:473–532

Kennett BLN (1980) Seismic waves in a stratified half space – II. Theoretical seismograms. Geophys J Int 61(1):1–10. https://doi.org/10.1111/j.1365-246X.1980.tb04299.x

Kind R (1977) The reflectivity method for a buried source. J Geophys 44:603–612

Kotha SR, Weatherill G, Bindi D, Cotton F (2020) A regionally-adaptable ground-motion model for shallow crustal earthquakes in Europe. Bull Earthq Eng 18(9):4091–4125. https://doi.org/10.1007/s10518-020-00869-1

Kotha SR, Bindi D, Cotton F (2022) A regionally adaptable ground-motion model for fourier amplitude spectra of shallow crustal earthquakes in Europe. Bull of Earthq Eng 20(2):711–740. https://doi.org/10.1007/s10518-021-01255-1

Kraft T, Deichmann N (2014) High-precision relocation and focal mechanism of the injection-induced seismicity at the Basel EGS. Geothermics 52:59–73. https://doi.org/10.1016/j.geothermics.2014.05.014, analysis of Induced Seismicity in Geothermal Operations

Landesamt für Geologie und Bergbau Rheinland-Pfalz (2020) LGB-Kartenviewer - Layer Erdbebenereignisse, Layer Geologische Übersichtskarte (GUEK 300). https://mapclient.lgb-rlp.de/. Accessed 24 June 2020

Landesamt für Geologie, Rohstoffe und Bergbau Baden-Württemberg, Regierungspräsidium Freiburg (2019) LGRB-Kartenviewer: Tektonische Erdbeben seit 1994, Geologische Einheiten (GÜK300). https://maps.lgrb-bw.de/. Accessed 30 Oct 2020

Lee WHK, Lahr JC (1972) HYPO71: a computer program for determining hypocenter, magnitude, and first motion pattern of local earthquakes. Tech rep. https://doi.org/10.3133/ofr72224, report

Leydecker G (2011) Erdbebenkatalog für die Bundesrepublik Deutschland mit Randgebieten für die Jahre 800 bis 2008. In: Geologisches Jahrbuch, Hannover, no. 59 in E, pp 1–198

Leydecker G, Aichele H (1998) The seismogeographical regionalisation for Germany: the prime example of third-level regionalisation. In: Geologisches Jahrbuch, Hannover, no. 55 in E, pp 85–98

Lokmer I, Bean CJ (2010) Properties of the near-field term and its effect on polarisation analysis and source locations of long-period (LP) and very-long-period (VLP) seismic events at volcanoes. J Volcanol Geotherm Res 192(1):35–47. https://doi.org/10.1016/j.jvolgeores.2010.02.008

McNamara DE (2000) Frequency dependent LG attenuation in south-central Alaska. Geophys Res Lett 27(23):3949–3952. https://doi.org/10.1029/2000GL011732

Mori J, Helmberger D (1996) Large-amplitude Moho reflections (SmS) from Landers aftershocks, Southern California. Bull Seismol Soc Am 86(6):1845–1852

Müller G (1985) The reflectivity method: a tutorial. J Geophys 58:153–174

Müller B, Zoback ML, Fuchs K, Mastin L, Gregersen S, Pavoni N, Stephansson O, Ljunggren C (1992) Regional patterns of tectonic stress in Europe. J Geophys Res Solid Earth 97(B8):11783–11803. https://doi.org/10.1029/91JB01096

Munafò I, Malagnini L, Chiaraluce L (2016) On the relationship between Mw and ML for small earthquakes. Bull Seismol Soc Am 106(5):2402–2408, issn=0037–1106, https://doi.org/10.1785/0120160130

Oncescu MC, Rizescu M, Bonjer KP (1996) SAPS - an automated and networked seismological acquisition and processing system. Computers & Geosciences 22(1):89–97. https://doi.org/10.1016/0098-3004(95)00060-7

Paris Institute of Earth Physics (IPGP), School and Observatory for Earth Sciences of Strasbourg (EOST) (1982) GEOSCOPE, French Global Network of broad band seismic stations. https://doi.org/10.18715/GEOSCOPE.G

QGIS Development Team (2009) QGIS Geographic Information System. Open Source Geospatial Foundation. http://qgis.org

Reicherter K, Froitzheim N, Jarosiński M, Badura J, Franzke HJ, Hansen M, Hübscher C, Müller R, Poprawa P, Reinecker J, Stackebrandt W, Voigt T, Eynatten HV, Zuchiewicz W (2008) Alpine tectonics north of the Alps. In: The Geology of Central Europe Volume 2: Mesozoic and Cenozoic, Geological Society of London, https://doi.org/10.1144/CEV2P.7

Résif-RLBP (1995) RESIF-RLBP French Broad-band network, RESIF-RAP strong motion network and other seismic

stations in metropolitan France. https://doi.org/10.15778/RESIF.FR
Ritter J (2017) DEEP-TEE Phase 2. https://doi.org/10.7914/SN/9Q_2017
Ritter J, Schmidt B, Haberland C, Weber M, Stange S, Lehmann K, Hensch M, Koushesh M (2019) The DEEP-TEE seismological experiment: exploring micro-earthquakes in the East Eifel Volcanic Field. Geophys Res Abstr 21(EGU2019-13615). https://meetingorganizer.copernicus.org/EGU2019/EGU2019-13615.pdf
Royal Observatory of Belgium (1985) Belgian Seismic Network. https://doi.org/10.7914/SN/BE
Sato R (1979) Theoretical basis on relationships between focal parameters and earthquake magnitude. Journal of Physics of the Earth 27(5):353–372. https://doi.org/10.4294/jpe1952.27.353
Schmittbuhl J, Lengliné O, Lambotte S, Grunberg M, Doubre C, Vergne J, Cornet F, Masson F (2020) A triggered seismic swarm below the city of Strasbourg, France on Nov 2019. No. EGU2020-18712 in EGU General Assembly 2020, https://doi.org/10.5194/egusphere-egu2020-18712
Schmittbuhl J, Lengline O, Lambotte S, Grunberg M, Doubre C, Vergne J, Cornet F, Masson F (2021) Induced and triggered seismicity from Nov 2019 to Dec 2020 below the city of Strasbourg. No. EGU21-8374 in EGU General Assembly 2021, https://doi.org/10.5194/egusphere-egu21-8374
Schneider G (1979) The earthquake in the Swabian Jura of 16 November 1911 and present concepts of seismotectonics. Tectonophysics 53(3):279–288. https://doi.org/10.1016/0040-1951(79)90072-6, proceedings of the 16th General Assemble of the European Seismological Commission
Service géologique national Bureau de Recherches Géologiques et Minières (2016) BRGM INSPIRE and OneGeology surface geology (WMS-Service). http://mapsref.brgm.fr/wxs/1GG/BRGM_1M_INSPIRE_geolUnits_ geolFaults?language=eng &. Accessed 24 July 2020
Stange S (2006) ML determination for local and regional events using a sparse network in Southwestern Germany. J Seismol 10(2):247–257. https://doi.org/10.1007/s10950-006-9010-6
State Seismological Service of Baden-Württemberg, Regierungspraesidium Freiburg (2009) State Seismological Service. Freiburg, Germany. https://doi.org/10.7914/SN/LE
State Seismological Service of Rhineland-Palatinate, Geological Survey of Rhineland-Palatinate (n.d.) State Seismological Service, Mainz, Germany
Sugan M, Vuan A (2012) Evaluating the relevance of Moho reflections in accelerometric data: application to an inland Japanese Earthquake. Bull Seismol Soc Am 102(2):842–847. https://doi.org/10.1785/0120110085
Sugan M, Vuan A (2014) On the ability of Moho reflections to affect the ground motion in northeastern Italy: a case study of the 2012 Emilia seismic sequence. Bull Earthq Eng 12(5):2179–2194. https://doi.org/10.1007/s10518-013-9564-y
Swiss Seismological Service (SED) At ETH Zurich (1983) National Seismic Networks of Switzerland. https://doi.org/10.12686/SED/NETWORKS/CH
Swiss Seismological Service (SED) at ETH Zürich: Federal Institute for Technology (2015) The Site Characterization Database for Seismic Stations in Switzerland. https://doi.org/10.12686/sed-stationcharacterizationdb, http://stations.seismo.ethz.ch. Accessed 30 Jan 2021
Terashima T (1968) Magnitude of microearthquakes and the spectra of microearthquakes. Bull Int Inst Seismol Earthq Eng 5:31–108, (citation after Sato, 1979)
Van Rossum G, Drake FL (2009) Python 3 Reference Manual. CreateSpace, Scotts Valley, CA
Virtanen P, Gommers R, Oliphant TE, Haberland M, Reddy T, Cournapeau D, Burovski E, Peterson P, Weckesser W, Bright J, van der Walt SJ, Brett M, Wilson J, Millman KJ, Mayorov N, Nelson ARJ, Jones E, Kern R, Larson E, Carey CJ, Polat I, Feng Y, Moore EW, VanderPlas J, Laxalde D, Perktold J, Cimrman R, Henriksen I, Quintero EA, Harris CR, Archibald AM, Ribeiro AH, Pedregosa F, van Mulbregt P, SciPy 10 Contributors (2020) SciPy 1.0: Fundamental algorithms for scientific computing in python. Nat Methods 17:261–272. https://doi.org/10.1038/s41592-019-0686-2
Yamaguchi N, Yamazaki K, Ikegami R (1978) The relationship between the predominant period and the magnitude for the earthquakes which occurred in and near the Kwanto district. Zisin (Journal of the Seismological Society of Japan 2nd ser) 31(2):207–227. https://doi.org/10.4294/zisin1948.31.2_207
Ziegler PA (1994) Cenozoic rift system of Western and Central Europe: an overview. Geologie en Mijnbouw 73(2–4):99–127